Global and Planetary Change
November 2023, Volume 230, Pages 104283 (13p.)
https://doi.org/10.1016/j.gloplacha.2023.104283 https://archimer.ifremer.fr/doc/00856/96833/

Glacial expansion of carbon-rich deep waters into the Southwestern Indian Ocean over the last 630 kyr

Pérez-Asensio José N. [1, *], Tachikawa Kazuyo [1], Vidal Laurence [1], De Garidel-Thoron Thibault [1], Sonzogni Corinne [1], Guihou Abel [1], Deschamps Pierre [1], Jorry Stephan [2], Chen Min-Te [3]

[1] Aix Marseille Univ., CNRS, IRD, INRAE, Coll France, CEREGE, Aix-en-Provence, France
[2] Geo-Ocean, UMR6538 Univ. Brest-CNRS-IFREMER, F-29280 Plouzané, France
[3] Institute of Earth Sciences & Center of Excellence for the Oceans & Center of Excellence for Ocean Engineering, National Taiwan Ocean University, Keelung 20224, Taiwan

* Corresponding author : José N. Pérez-Asensio, email address : jnperezasensio@gmail.com

kazuyo@cerege.fr ; vidal@cerege.fr ; garidel@cerege.fr ; sonzogni@cerege.fr ; guihou@cerege.fr ; deschamps@cerege.fr ; stephan.jorry@ifremer.fr ; mtchen@mail.ntou.edu.tw

Abstract :

Oceanic carbon storage is one of the main sinks for atmospheric CO2, and thought to be the major contributing factor for CO2 drawdown during past glacial periods. Both physical and biogeochemical processes control the capacity of carbon storage in the ocean. During glacial periods of the Pleistocene the larger volume of deep-water masses of Southern Hemisphere origin in the Atlantic has been shown to promote carbon storage in the Southern Ocean. However, the latitudinal extension of this water mass in the Indian Ocean has been scarcely studied. In this study, we combine foraminiferal εNd and benthic δ13C of two sediment cores in the southwest Indian Ocean (MD96–2077, 33°S, 3781 m water depth; MD96–2052, 19°S, 2627 m water depth), to reconstruct the spatial and temporal evolution of glacial carbon-rich deep waters in the SW Indian over the last 630 kyr. The combined use of foraminiferal εNd and benthic δ13C allows to distinguish δ13C changes related to water mass mixing and from respired carbon accumulation within the water masses. Nutrient-rich deep waters, which cannot be explained by the enhanced proportion of southern-sourced waters, were present at core sites deeper than 2700 m during glacial periods and extended at least until 33°S into the SW Indian Ocean. From Marine Isotope Stage (MIS) 14 to MIS 10, glacial carbon storage increased gradually until reaching its highest capacity during the extreme glacial periods MIS 12 and 10. Orbital forcing (100-kyr eccentricity, 41-kyr obliquity), restricted air-sea exchange and enhanced ocean stratification, fostered higher carbon storage during periods of relatively lower eccentricity and obliquity. Furthermore, after MIS 10, a progressive transition was observed from 100-kyr eccentricity to 41-kyr obliquity cycles in benthic δ13C and δ18O records of core MD96–2077 and sea-ice cover changes derived from ice-rafted debris of the Agulhas Plateau composite core site.

Highlights

► Analysis of authigenic ε_{Nd} and benthic $\delta^{13}C$ were combined for the last 630 kyr. ► Glacial C-rich deep waters were present below 2700 m extending into the SW Indian. ► Glacial carbon storage increased during low eccentricity and obliquity. ► C storage changed gradually from 100-kyr eccentricity to 41-kyr obliquity cycles.

Keywords : Carbon cycle, Neodymium isotopes, carbon isotopes, glacial-interglacial cycles, Pleistocene, Indian Ocean

1. Introduction

Ocean carbon cycle plays a fundamental role in sequestering CO_2 during glacial periods (Sarmiento and Toggweiler, 1984; Stephens and Keeling, 2000; Sigman et al., 2010). Glacial ice sheets on land, contributing to increased aridity and colder temperatures, reduced terrestrial carbon storage (Peterson et al., 2014). This resulted in most of the terrestrial carbon stored in the ocean, which is the largest carbon reservoir. The Last Glacial Maximum (LGM) to Holocene global ocean $\delta^{13}C$ ($^{13}C/^{12}C$ carbon isotopic composition) change was 0.34 ± 0.19‰, implying an oceanic carbon variation of 330–694 Gt C (Peterson et al., 2014). One of the most important regions regarding the oceanic carbon cycle is the Southern Ocean, where under glacial conditions higher seawater CO_2 solubility, larger sea-ice, restricted air-sea exchange, stronger ocean stratification, sluggish deep-water circulation and enhanced nutrient utilization, reduced atmospheric CO_2 and favored ocean carbon storage (Sigman and Boyle, 2000; Stephens and Keeling, 2000; Sigman et al., 2010; Adkins, 2013; Lear et al., 2016; Lhardy et al., 2021). During glacial periods, larger ice sheets along with higher iron fertilization enhancing nutrient utilization and low air-sea exchange resulted in reduced $\delta^{13}C$ of dissolved inorganic carbon ($\delta^{13}C$-DIC) (Mix and Fairbanks, 1985; Gebbie, 2014). Indeed, in the Atlantic sector of the Southern Ocean, deep-water (> 3000 m) benthic foraminiferal $\delta^{13}C$ glacial values were lower than those of the deep equatorial Pacific (Mix et al., 1995; Hodell et al., 2003), suggesting an important role of the Southern Ocean to storage of respired carbon. More extensive sea ice cover combined with ocean stratification in the Southern Ocean may reduce the atmospheric CO_2 by 40 ppm (Stein et al., 2020). It has been proposed, based on benthic $\delta^{13}C$ records, that glacial carbon-rich Southern Ocean waters might have extended into the abyssal North Atlantic during the LGM in relation to weaker and shallower North Atlantic Deep Water (NADW) (Curry and Oppo, 2005; Gebbie, 2014). However, sustained production of NADW was suggested during the LGM from foraminiferal

authigenic Nd isotopic composition ($^{143}Nd/^{144}Nd$ or ε_{Nd}) (Howe et al., 2016). Discrepancies of proxy reconstructions imply that reduced glacial NADW alone cannot fully explain the increased oceanic carbon storage. Different models reconstructing LGM circulation and related CO_2 drawdown also show discrepancies due to model resolution, simulation of ocean circulation and climate, representation of atmosphere and ocean physics and carbon cycle model completeness (Lhardy et al., 2021).

Glacial deep waters with a significant amount of respired carbon might have extended into other oceans in addition to the Atlantic Ocean, increasing their volume (Ferrari et al., 2014). Expanded southern-sourced nutrient-rich deep waters may enhance the total marine carbon inventory by trapping more CO_2 during glacial periods (Skinner, 2009). The Indian Ocean is one of the areas in which glacial carbon-rich waters could have arrived since southern-sourced waters, such as Circumpolar Deep Water (CDW), bath the southwestern part of this ocean (Fig. 1). To test if glacial deep waters, enriched in respired carbon, extended to the SW Indian, one of the most insightful approaches is to combine authigenic ε_{Nd} and benthic foraminiferal $\delta^{13}C$ records from deep water sites from the SW Indian. The present-day seawater ε_{Nd} values at water depths greater than 1500 m trace water-mass provenances and behave semi-conservatively when the influence of local inputs is small (e.g. Goldstein and Hemming, 2003; Tachikawa et al., 2017). Benthic $\delta^{13}C$ reflects different factors including organic carbon export and remineralization, respired carbon accumulation and air-sea exchange (Mix and Fairbanks, 1985; Howe et al., 2016). Therefore, combining benthic $\delta^{13}C$ with ε_{Nd} will allow distinguishing $\delta^{13}C$-DIC changes related to water mass mixing from those produced by respired carbon accumulation.

In order to investigate the extension of carbon-rich deep waters under different mean climate states, it is necessary to obtain records covering several glacial-interglacial cycles. Climate states, with different average temperatures, may have modified differently ocean

carbon storage, and, therefore, extension of carbon-rich deep waters. Previous studies of deep-water (>2500 m) benthic $\delta^{13}C$ records from the SW Indian are scarce (Pichon et al., 1992; Ziegler et al., 2013), and to date, the combination of $\delta^{13}C$ and ε_{Nd} covering several climate cycles has never been realized.

Here, we present new combined foraminiferal ε_{Nd} and epibenthic foraminiferal $\delta^{13}C$ records from two sites in the SW Indian Ocean over the past 630 kyr (Fig. 1): 1) core MD96-2077 (33°10.1'S, 31°14.8'E, 3781 m water depth), and 2) core MD96-2052 (19°52.7'S, 41°49.9'E, 2627 m water depth). This time interval covers different climate states, including extreme glacial conditions during MIS10 and 12 (Bard and Rickaby, 2009). The benthic $\delta^{13}C$ and foraminiferal authigenic ε_{Nd} relationship permitted distinguishing changes in water-mass contributions from ventilation and related accumulation of respired carbon. These new data, together with previously published benthic $\delta^{13}C$ records, allowed us to define the vertical and horizontal extension of glacial carbon-rich deep waters entering the SW Indian, which can contribute to the modification of marine carbon inventory and, consequently, oceanic CO_2 uptake.

2. Present-day deep-water circulation

In the study area, two main deep-water currents flow from the SE Atlantic to the SW Indian Ocean: the shallower North Atlantic Deep Water (NADW), and the deeper Circumpolar Deep Water (CDW) (Fig. 1). In the present SW Indian Ocean, the southern-sourced water at deep water depths of locations northern than 50ºS is essentially lower circumpolar deep water (CDW) according to neutral density distribution (Orsi et al., 1999). Antarctic Bottom Water (AABW) flows in the deepest part of the Indian Ocean below 3800 m, entering the Mozambique basin (SW of Madagascar) (Tomczak and Godfrey, 1994) (Fig.

1a). This water mass formation results from brine rejection during sea ice formation or super-cooling of ice shelf water (Carmack and Foster, 1975).

The NADW, with higher salinity and potential temperature, occurs between 2000 and 3500 m (Figs. 1b and 2). This water mass is formed in the North Atlantic Ocean. It travels southward along the western Atlantic until it bifurcates around the equator into two branches, one flowing in the western Atlantic and the other flowing in the eastern Atlantic (Larqué et al., 1997). Around 40°S, the eastern branch deflects to the east, entering the SW Indian Ocean (Larqué et al., 1997). The NADW is part of the upper overturning cell of the Atlantic Meridional Overturning Circulation (AMOC) (Kuhlbrodt et al., 2007). In the SW Indian Ocean, the NADW flows northward, entering the Mozambique Channel (de Ruijter et al., 2002). It deflects and turns south at around 20°S (Charles et al., 2020) (Fig. 1a). The CDW is found deeper than 3500 m (Fig. 1b) and divided into Upper and Lower CDW (UCDW, LCDW), with LCDW being colder and saltier than UCDW (Fig. 2). The CDW is colder and fresher than NADW (Figs. 1a and 2). The origin of CDW is the mixing of NADW, Indian and Pacific deep waters, along with the local Antarctic dense waters (Talley, 2013). The CDW enters the Indian Ocean from the SE Atlantic, flowing along the SW coast of S Africa (Fig. 1a). It also flows northward from the Southern Ocean to the Indian Ocean along the eastern side of Madagascar (Fig. 1a). At the present day, the potential temperature-salinity diagram and water-mass properties (Amakawa et al., 2019) reveal that core MD96-2077 location is affected by LCDW, while the core MD96-2052 location is bathed by the NADW (Fig. 2).

3. Material and methods

3.1. Studied cores

3.1.1. Core MD96-2077

Sediment core MD96-2077 was collected off East London in the Natal Valley (SW Indian Ocean, 33°10.1'S, 31°14.8'E, 3781 m water depth) (Fig. 1). The core is 3554 cm long and mainly composed of biogenic carbonates (coccoliths and foraminifera) (Bertrand and Shipboard Scientific Party, 1997; Chen et al., 1998). The chronology of this core was initially constrained by *Globoconella inflata* $\delta^{18}O$ record (Bard and Rickaby, 2009). We refined the age model by a new benthic foraminiferal *Cibicidoides wuellerstorfi* $\delta^{18}O$ record and a new ^{14}C date on *G. inflata* from the uppermost part of the core (Fig. A.1 and Table B.1). The benthic foraminiferal $\delta^{18}O$ record was tuned to the LR04 global stack (Lisiecki and Raymo, 2005) (Fig. A.1). The age model is based on linear interpolation using 25 tie points, one based on radiocarbon dating and 24 based on benthic $\delta^{18}O$ stratigraphy (Table B.1). The radiocarbon age was calibrated using the Marine20 calibration curve (Heaton et al., 2020), with a ΔR value of -21±26 yr and 400 yr marine reservoir age. Here, we analyzed the upper 2401 cm of the core, covering the last 630 kyr according to our age model. This interval shows an average sedimentation rate of 4.5 cm/kyr.

3.1.2. Core MD96-2052

Sediment core MD96-2052 was retrieved off Madagascar in the Mozambique Channel (SW Indian Ocean, 19°52.7'S, 41°49.9'E, 2627 m water depth) (Fig. 1) during the MOZAPHARE cruise (R/V MD, 1996). This 3754-cm-long core consists of biogenic sediments rich in coccoliths and foraminifera (Lancelot and Shipboard Scientific Party, 1997). This core was dated using radiocarbon dating on the planktic foraminifera *Globigerinoides ruber* and tuning the benthic foraminiferal *Cibicidoides wuellerstorfi* $\delta^{18}O$ record to the benthic LR04 global stack (Lisiecki and Raymo, 2005) (Figs. A.2 and A.3). The age model was constructed using 28 tie points, 7 ^{14}C dates and 21 benthic $\delta^{18}O$ tie points

(Table B.2). In the uppermost part of the core (0-480 cm) (Fig. A.3), the age model was established with the Bayesian statistics software Bacon v2.3 (Blaauw and Christen, 2011) using the statistical package RStudio v4.1.1. The radiocarbon ages were calibrated using the Marine20 calibration curve (Heaton et al., 2020), with a ΔR value of 108±51 yr and 400 yr marine reservoir age. In the rest of the core (480-3140 cm) (Fig. A.2), the age model is based on linear interpolation using the 21 benthic $\delta^{18}O$ tie points. The upper 3140 cm of the core, representing the last 575 kyr, were studied. The average sedimentation rate for this interval is 7.7 cm/kyr.

3.2. Methods

3.2.1. Nd isotopes of cleaned mixed planktic foraminifera

Samples for Nd isotopic analyses on mixed planktic foraminifera were selected to cover glacial-interglacial variability of core MD96-2077 (Fig. 3b), with a sampling resolution of 13.8 ka along the studied interval and higher resolution (3.9 ka) during terminations I (MIS 1-2), II (MIS 6-5) and V (MIS 12-11) (Fig. 3b). For core MD96-2052, we focused on terminations I, II and V (Fig. 3b), with a resolution per sample of 3.4 kyr within terminations. Terminations I, II and V were analyzed in detail because Terminations I, II and V are related to the warmest interglacials and characterized by large glacial-interglacial amplitudes (Fig. 3a). For the ε_{Nd} analyses, 20-50 mg of mixed planktic foraminifera from the size fraction >250 µm were picked. Most of the samples were automatically picked by MiSo (Microfossil Sorter) prototype (26 samples in core MD96-2077, and 29 samples in core MD96-2052), a novel device developed at CEREGE, which images sediment coarse fraction, identifies particles and foraminifera using Convolutional Neural Networks (Marchant et al., 2020), and picks microfossils for subsequent geochemical analyses (patent pending).

Additionally, samples were handpicked to complete the picking of selected samples (20 samples in core MD96-2077, and 2 samples in core MD96-2052).

Prior to the measurements of Nd isotopic composition, foraminiferal tests were mechanically cleaned with the established method summarized in Tachikawa et al. (2014). Briefly, foraminiferal chambers were gently crushed using two glass slides under the binocular stereo microscope. Fine particles, including clays, were removed by repeated ultrasonication steps until the water was clear. Carbonate test fragments were dissolved by step-wise addition of 1M acetic acid. The obtained solution was centrifuged, and the recovered supernatant was evaporated and attacked with concentrated nitric acid. Then, samples were purified by a 2-step column separation using TRU.Spec and Ln.Spec resins to isolate Nd (Pin and Santos Zalduegui, 1997).

Nd isotopic composition was measured using a Thermo Fisher Neptune^{Plus} Multi-Collector Inductively Coupled Plasma Mass Spectrometer (MC-ICP-MS) at CEREGE. The sample size was around 10 ng of Nd. An Apex Omega Quartz desolvation device was used for sample introduction. To correct instrumental mass bias, $^{143}Nd/^{144}Nd$ were firstly normalized internally to a $^{146}Nd/^{144}Nd$ of 0.7219 after correcting for any Sm interferences. Secondly, the $^{143}Nd/^{144}Nd$ were corrected by bracketing every sample with the JNdi-1 isotopic standard solutions obtained from a neodymium oxide reagent ($^{143}Nd/^{144}Nd$ = 0.512115 ± 0.000007, Tanaka et al. (2000)). The JNdi-1 standard solutions were analyzed at the same concentrations as the samples. The sample uncertainties reported in Table B.3 were calculated by error propagation of the standard error of the sample and the ones of the bracketing standards (assuming independent variables). It is reported as 2σ. The average uncertainty is 0.3 ε-unit (Table B.3), in agreement with the external reproducibility (2SD) of the JNdi-1 standard, 0.27 ε-unit as well as the ones obtained on complete procedural replicate analyses of several samples (see Table B.3). Repeated measurements of the AMES

($^{143}Nd/^{144}Nd$ = 0.511961 ± 0.000008) and VWR ($^{143}Nd/^{144}Nd$ = 0.512177 ± 0.000006) standard solutions were carried out to check the accuracy of the analyses. Procedural blank values were <100 pg and were therefore neglected as they represented less than 1% of the Nd analyzed per sample.

3.2.2. Benthic foraminiferal stable isotope measurements

For benthic oxygen and carbon stable isotope measurements of cores MD96-2077 and MD96-2052, 2-4 shells of the epibenthic foraminifer *C. wuellerstorfi* (250-355 µm size fraction) were picked. The $\delta^{13}C$ and $\delta^{18}O$ signature of *C. wuellerstorfi* was measured on an IRMS Delta V-Plus (Thermo-Finnigan) equipped with a carbonate preparation device (Carbo-Kiel IV) at CEREGE. The standard NBS19 was used to normalize measured isotopic values. Mean external reproducibility (1SD) was better than 0.07‰ for $\delta^{18}O$ and 0.03‰ for $\delta^{13}C$. The resolution per sample was respectively 4.3 kyr and 2.2 kyr for cores MD96-2077 and MD96-2052.

4. Results

4.1. Foraminiferal ε_{Nd} records

The foraminiferal core-top ε_{Nd} value of core MD96-2077 is -10.2 ± 0.2 at 7.3 ka (Fig. 3b and Table B.3). Since no data on seawater Nd isotopic composition are available at site MD96-2077, we compare the core-top value with the seawater ε_{Nd} value estimated by an empirical equation using seawater PO_4, SiO_2, salinity, and temperature values from World Ocean Atlas 2018 (WOA18) (Tachikawa et al., 2017; Boyer et al., 2018). The core-top value (-10.2 ± 0.2) is close to the estimated seawater ε_{Nd} value of -9.9. Over the last 630 kyr, the ε_{Nd} record of core MD96-2077 ranges from -11.1 ± 0.3 (MIS 11) to -8.0 ± 0.3 (MIS 12), with

generally more radiogenic values (i.e. higher) during glacial periods and less radiogenic values (i.e. lower) during interglacial periods (Fig. 3b).

The average core-top ε_{Nd} value of core MD96-2052 is -11.9 ± 0.2 at 2.8 ka based on 3 replicate analyses (Fig. 3b and Table B.3). This value is in good agreement with the typical modern NADW seawater ε_{Nd} value of -12.3 ± 0.9 in the N Atlantic (Tachikawa et al., 2017) (Fig. 3b). The core-top ε_{Nd} value is also similar to the seawater ε_{Nd} value of -10.8 estimated at MD96-2052 site using the previously described empirical equation. The ε_{Nd} record of this core along terminations I, II, and V ranges from -12.3 ± 0.2 (MIS 11) to -9.4 ± 0.5 (MIS 6), with more radiogenic glacial values and less radiogenic interglacial values (Fig. 3b).

4.2. Benthic foraminiferal $\delta^{18}O$ and $\delta^{13}C$ records

At core MD96-2077, the benthic $\delta^{18}O$ values range from 2.29 (MIS 5) to 4.51‰ (MIS 12), with heavier values during glacial periods and lighter values during interglacial periods (Fig. 3a and Table B.4). In core MD96-2052, the benthic $\delta^{18}O$ record ranges from 2.31 (MIS 5) to 5.04‰ (MIS 12), with heavier glacial values than interglacial values (Fig. 3a and Table B.4). The average benthic $\delta^{18}O$ of core MD96-2077 (3.64±0.46‰) is very similar to the average $\delta^{18}O$ value of core MD96-2052 (3.55±0.53‰), which is shown by the close correlation of both records (Fig. 3a).

Concerning the benthic $\delta^{13}C$ records, values at core MD96-2077 range from -1.08 (MIS 8) to 0.69‰ (MIS 11), with more depleted values during glacial periods (Fig. 3c and Table B.4). A trend towards generally more depleted glacial values from MIS 14 to MIS 10 is observed (Fig. 3c). The benthic $\delta^{13}C$ values at core MD96-2052 range from -0.16 (MIS 10) to 1.24‰ (MIS 11 and 13). The average benthic $\delta^{13}C$ value of core MD96-2077 (-0.15±0.39‰) is much more depleted than the average $\delta^{13}C$ value (0.60±0.30‰) of core MD96-2052.

5. Discussion

Deep-water authigenic foraminiferal ε_{Nd} values mostly reflects water mass provenance and mixing; however, local Nd source such as boundary exchange can also modify authigenic ε_{Nd} values. We estimated that the influence of unradiogenic ε_{Nd} from boundary exchange is negligible at the two sites based on the following reasons. Firstly, as shown in Fig. 3b, the core-top ε_{Nd} values of both cores are close to the compiled or expected modern seawater ε_{Nd} (Tachikawa et al., 2017 and references therein). Secondly, detrital ε_{Nd} values at MD96-2052 and MD96-2077 sites are about -15 and -10, respectively (Robinson et al., 2021) and the contribution of local Nd sources with these low ε_{Nd} (including Limpopo and Zambezi) cannot explain the observed more radiogenic glacial signals. The ε_{Nd} difference between the two sites is ~1 ε-unit (figure 3b) can be better explained by the presence of different water masses (NADW in core MD96-2052 and CDW in core MD96-2077) (see figure 1b).

The two studied ε_{Nd} records indicate clear glacial-interglacial changes. The benthic foraminiferal $\delta^{13}C$ records of the two cores also show glacial-interglacial cycles with always more depleted values for core MD96-2077, particularly during glacial periods. The higher authigenic ε_{Nd} values and lower benthic foraminiferal $\delta^{13}C$ during glacial periods have been interpreted as an enhanced proportion of southern-sourced water represented by glacial CDW with possible contribution of glacial AABW (Starr et al., 2021). To determine which amount of the benthic foraminiferal $\delta^{13}C$ changes can be explained by water mass mixing and what is the amount of additional depletion of $\delta^{13}C$, we focus on the relationship between authigenic ε_{Nd} and benthic $\delta^{13}C$ data.

5.1. Accumulation of respired carbon in deep glacial Indian water inferred from ε_{Nd}-$\delta^{13}C$ signatures

Since the present-day water masses occupying the core sites MD96-2052 and MD96-2077 are NADW and CDW, respectively, we consider binary mixing between the two water masses, defined by the present-day NADW and CDW endmembers values of ε_{Nd} and δ^{13}C-DIC (Key et al., 2004; Schmittner et al., 2013; Tachikawa et al., 2017) (Fig. 4). If the paired ε_{Nd}-δ^{13}C data of the cores are on the defined mixing envelop, the changes in authigenic foraminiferal ε_{Nd} and benthic foraminiferal δ^{13}C data can be considered to reflect the different mixing proportion between the northern-sourced (NSW) and southern-sourced (SSW) without additional accumulation of respired carbon in the water masses. This is the case with Holocene values for the two studied cores as well as ODP Site 1090 (3702 m water depth) in the SE Atlantic Ocean (Hodell et al., 2003; Pena and Goldstein, 2014) and the equatorial Indian core SK129-CR2 (3°N, 76°E, 3800 m water depth) (Piotrowski et al., 2009), located deeper than 2700 m and bathed by the Upper Circumpolar Deep Water (UCDW) (Figs 1 and 4).

During glacial periods, ε_{Nd}-δ^{13}C values of both NSW and SSW could be different from those of the modern ocean (Fig. 4). The glacial binary mixing is evaluated assuming that the glacial NSW corresponded to the Glacial North Atlantic Intermediate Water (GNAIW), a water mass resulting from the shallowing of NADW during glacial periods, and the glacial SSW was composed of Glacial Pacific Deep Water (GPDW) with potential contribution of Glacial Antarctic Bottom Water (GAABW) (Starr et al., 2021). The properties of these endmembers are estimated by Yu et al. (2020) for the LGM: GNAIW is characterized by ε_{Nd} ranging from -13.5 to -10.5 and a δ^{13}C of +1.5‰; GPDW has ε_{Nd} of -3.5 and δ^{13}C of -0.4‰; GAABW has ε_{Nd} of -6.7 and δ^{13}C of -0.83‰ (Yu et al., 2020). Dissolved inorganic carbon and dissolved Nd concentration of each member are also from (Yu et al., 2020). We are aware that the estimated glacial endmember values contain uncertainty and the

LGM does not represent the whole studied glacial periods. We thus consider the uncertainty of the endmember properties equivalent to the modern values (Fig. 4).

Using the glacial binary mixing line, we observe that glacial benthic $\delta^{13}C$ values of core MD96-2077 (3781 m water depth) are more depleted than the expected values from the glacial binary mixing line (Fig. 4). A closer look at the ε_{Nd}-$\delta^{13}C$ relationship of MD96-2077 data reveals the following points: 1) the majority of glacial values from core MD96-2077 are found below the glacial binary mixing line (Fig. 4); and 2) few interglacial values are also below the glacial binary mixing line, but they are evaluated to be influenced by high organic matter fluxes (inferred by high Total Organic Carbon (TOC) and *Globigerina bulloides* abundance) or cold climate substage conditions within interglacial periods, which favored depleted benthic $\delta^{13}C$ (Figs. 4 and A.4). The observed glacial ε_{Nd}-$\delta^{13}C$ relationship for cores MD96-2077 and ODP1090 is difficult to explain without accumulation of respired carbon. Only direct mixing between GNAIW and GAABW without GPDW contribution could partly account for the depleted $\delta^{13}C$, but such a mixing is improbable considering the rapid dilution of AABW during northward flow by CDW and the absence of GAABW originated from the Weddell Sea (Huang et al., 2020). The glacial ε_{Nd}-$\delta^{13}C$ relationship with low $\delta^{13}C$ for cores MD96-2077 and ODP1090 contrasts well with the trend of MD96-2052 and SK129-CR2, more closely located on the glacial binary mixing (Fig. 4).

It is interesting to note that even more depleted epibenthic $\delta^{13}C$ values relative to the glacial binary mixing were also observed for ODP Site 1090 (3702 m water depth) in the SE Atlantic Ocean (Hodell et al., 2003; Pena and Goldstein, 2014) (Fig. 4), also indicating accumulation of respired carbon in the bottom water in the SE Atlantic (Tachikawa et al., 2021). Thus, as carbon-rich deep waters (i.e. high in respired carbon) were found in both the deep SE Atlantic and SW Indian, we propose a northward extension of carbon-rich southern-sourced deep water into the SW Indian at site MD96-2077, with a vertical boundary between

2700 and 3700 m. In the southernmost sector (>46°S) of the SW Indian Ocean and the studied MD96-2077 core site (33ºS), authigenic uranium concentration data from several cores point toward poorly-ventilated carbon-rich waters below 2500 m (Bard and Rickaby, 2009; Amsler et al., 2022), consistent with our findings. In addition, presence of corrosive deep waters in the SW Indian Ocean during the LGM (Zhang et al., 2022) supports the inferred influence of carbon-rich deep waters below 2700 m in the SW Indian.

5.2. Spatial expansion of glacial carbon-rich deep waters in the SW Indian Ocean

Paired analysis of foraminiferal authigenic ε_{Nd} and benthic foraminiferal $\delta^{13}C$ fingerprints depleted glacial benthic $\delta^{13}C$ caused by the accumulation of respired carbon in the deep ocean, which in turn could help to estimate the water volume affected by oceanic carbon storage. Currently, only a limited number of data sets are available for the combined analysis of authigenic ε_{Nd} and epibenthic $\delta^{13}C$ records. Here, we try to evaluate the possible extension of glacial carbon-rich deep waters in the Indian Ocean, following the modern flow path of deep currents in the study area (Fig. 1a) based on a synthesis of benthic $\delta^{13}C$ records from the South Indian Ocean. Special attention is paid to water depths of cores and benthic $\delta^{13}C$ values relative to global stacked $\delta^{13}C$ values (Hoogakker et al., 2006) (Fig. 5). We compare several benthic $\delta^{13}C$ records from cores retrieved at different water depths in the SW and S Indian Ocean (Figs. 5 and 6), including cores MD96-2077 and MD96-2052 (this study), core MD02-2588 (SW Indian Ocean, 41°19.9'S, 25°49.7'E, 2907 m water depth) (Ziegler et al., 2013), and core MD84-527 (S Indian Ocean, 43°49'3S, 51°19'1E, 3262 m water depth) (Pichon et al., 1992).

The comparison of SW and S Indian benthic $\delta^{13}C$ records and the stacked benthic $\delta^{13}C$ curve reveals that the cores from water depths deeper than around 2700 m are characterized by benthic foraminiferal $\delta^{13}C$ values in the same range of the stacked values

only during interglacials (Fig. 5). During glacial periods, benthic $\delta^{13}C$ values of these deep cores never reach the level of the stacked values. If depleted benthic $\delta^{13}C$ values during glacials are indicative of carbon-rich waters, then these waters extended to depths deeper than 2700 m between 25ºE and 51ºE until 33°S along the S coast of Africa in the S. Indian Ocean (Figs. 5 and 6). Our interpretation is consistent with previously reported presence of carbon-rich waters below 2500 m in the SW Indian at latitudes >46°S (Amsler et al., 2022). The equatorial Indian core SK129-CR2 (3°N, 76°E, 3800 m water depth) (Piotrowski et al., 2009) shows glacial ε_{Nd}-$\delta^{13}C$ values, which are closely located on glacial binary mixing line between GNAIW and GPDW (Fig. 4). This reveals that glacial carbon-rich deep waters did not reach the equatorial Indian Ocean (Fig. 6).

We propose a tentative route for the extension of glacial carbon-rich deep waters in the central part of the study area, flowing northward into the Mozambique Channel (Fig. 6). Additional benthic foraminiferal $\delta^{13}C$ records from deep core sites in the SW Indian Ocean will be helpful to better depict the horizontal extension of these glacial deep waters with high accumulation of respired carbon.

5.3. Processes controlling deep-water carbon storage

To study processes controlling deep-water carbon storage in the South Indian, we at first compare global long-term background fluctuations of $\delta^{13}C$ and the benthic $\delta^{13}C$ record from various sites (Fig. 5). We assume that the long-term background $\delta^{13}C$ changes can be represented by the global stacked benthic $\delta^{13}C$ values (Hoogakker et al., 2006). As shown in Fig. 5, the stacked $\delta^{13}C$ has much smaller variability than benthic foraminiferal $\delta^{13}C$ changes at site MD96-2077. The larger amplitude of benthic $\delta^{13}C$ reflects the regional/local changes in ventilation, air-sea exchange of CO_2, and biological organic fluxes to the seafloor.

The ε_{Nd}-$\delta^{13}C$ combination allows distinguishing $\delta^{13}C$ changes related to water-mass mixing and deep-water carbon storage. Yet, the estimated storage is associated with both biological and physical processes without any distinction. It was proposed that biological and physical processes contributed to atmospheric CO_2 decline about 50% each (Hain et al., 2010). Thus, glacial carbon storage in the SW Indian resulted from the combination of biological processes (biological pumping) and physical processes (air-sea exchange, water stratification) in addition to higher proportion of carbon-rich SSW relative to the NSW.

The biological and physical processes controlling ocean carbon storage might be modulated by orbital forcing. To evaluate the influence of orbital cycles on carbon storage and related ice-sheets dynamics, spectral and wavelet analyses were performed using the software PAST (Hammer et al., 2001). The corrected benthic $\delta^{13}C$ record of core MD96-2077 shows significant spectral peaks with periodicities of 100 kyr (eccentricity) and 23 kyr (precession) for the whole studied interval (Fig. 7a). Furthermore, higher carbon storage (lower corrected benthic $\delta^{13}C$) occurred at times of relatively lower eccentricity and obliquity within glacial periods (see A-F red rectangles in Fig. 8b, 8c, and 8d). These findings support that orbital forcing could have influenced the extension and reduction of the nutrient-rich deep waters, and related ocean carbon storage. Orbital forcing governed the waxing and waning of polar ice sheets due to linear response to changes in high-latitude insolation for 41 and 23-kyr cycles and due to nonlinear response of the cryosphere for 100-kyr cycles (Hays et al., 1976; Shackleton, 2000). During glacial periods, more extended Antarctic sea ice was reconstructed by multi-proxy records for the last 130 kyr (Crosta el al., 2022 and references therein). The larger sea-ice could restrict air-sea exchange of CO_2 (Mix and Fairbanks, 1985; Sigman and Boyle, 2000; Gebbie, 2014) and similar reduction of air-sea exchange could have occurred during glacial periods of the last 630 kyr. Moreover, stronger density stratification in the Antarctic Zone waters during glacial periods would have also favored the accumulation

of respired carbon in the deep ocean (Hasenfratz et al., 2019). Sea-ice expansion promoted higher vertical density stratification through brine rejection during glacial periods. This ocean stratification played a dominant role in increasing CO_2 sequestration during the early stages of glacial cycles (Stein et al., 2020). For example, sea-ice driven stratification fostered higher C storage in the Cape Basin (Southern Ocean) during glacial periods (Hines et al., 2021). A modelling study shows that glacial atmospheric cooling can predict Antarctic bottom water isolation due to reduced air-sea exchange under larger sea ice and weaker mixing with NADW during LGM, explaining half of the glacial atmospheric CO_2 drawdown (Marzocchi and Jansen, 2019). Finally, glacial enhanced biological pumping, favored by dust-driven iron fertilization, and the equatorward migration of glacial westerlies and/or weaker westerlies would have also contributed to accumulate carbon in the deep ocean (Mix and Fairbanks, 1985; Gebbie, 2014; Sigman et al., 2010, 2021; Toggweiler et al., 2006). All these physical and biological processes might have enhanced the CO_2 sequestration capacity of glacial deep waters.

In addition to orbitally-controlled fluctuations in the ice-sheet and sea ice extension, changes in ocean circulation, including NADW reduction and poorly ventilated SSW, may have also contributed to promoting the extension of glacial carbon-rich waters. More radiogenic ε_{Nd} during glacial periods could support both weaker glacial NADW formation and/or relatively active glacial CDW flow compared to glacial NADW, both accounting for a higher influence of carbon-rich deep waters in the SW Indian (Fig. 4). Recently, Starr et al. (2021) suggested that a northward shift in iceberg trajectories during glacial periods led to much more meltwater spreading northward. This mechanism reduced salinity in surface waters flowing towards the North Atlantic and, therefore, weakened AMOC strength and/or favored occupation of shallower water depths, thus reducing the proportion of northern-sourced water in the binary mixing (Fig. 4). This other process might have indirectly

promoted the development of glacial carbon-rich deep waters, along with the previously discussed processes.

Assuming that the temporal evolution of carbon storage capacity of the deep S Indian ocean over the last 630 kyr, including both reduced ventilation and water mass mixing, can be monitored using the corrected benthic $\delta^{13}C$ curve from core MD96-2077 (Fig. 8d), we compare variations in the main forcing mechanisms such as orbital forcing and related sea-ice cover extension, which may be reconstructed using orbital curves (eccentricity and obliquity), the relative abundance of the diatom species *Fragilariopsis curta* and *F. cylindrus* at core SK200/33 located in the west Indian Ocean sector (Chadwick et al., 2022), and ice-rafted debris mass-accumulation rate (IRD_{MAR}) at Agulhas Plateau (AP) composite site (Figs. 1a and 8). A northward shift of IRD trajectories, indicated by higher IRD_{MAR} at the AP composite site, points to a more extensive sea-ice cover (Starr et al., 2021). The validity of this indirect proxy for sea-ice cover extension is supported by the positive correlation between higher IRD_{MAR} and higher abundances of the diatom species *F. curta* and *F. cylindrus* from west Indian core SK200/33, which indicate larger sea ice cover (Chadwick et al., 2022) (Fig. 8d). Over the last 630 kyr, the most conspicuous feature is the progressively decreasing of corrected benthic $\delta^{13}C$ from MIS 14 to MIS 10, suggesting gradually higher C storage capacity (Fig. 8d). The effect of local productivity influences on this trend was estimated to be minor since the highest surface productivity (inferred from *G. bulloides* abundance (Chen, 1996 [dataset]), the related highest organic matter accumulation and preservation (based on TOC and alkenones in bulk sediment) and seafloor oxygen decrease (deduced by authigenic uranium content) (Bard and Rickaby, 2009), occurred at the end of glacial periods (Fig. A.4). In contrast, corrected benthic $\delta^{13}C$ values decreased across glacial inceptions (Fig. A.4), revealing that carbon-rich deep waters arrived at the SW Indian at the beginning of glacial periods. Interglacial to glacial $\delta^{13}C$ change was 0.5, 1.3, and 1.6‰ for

glacial MIS 14, 12, and 10, respectively. Therefore, carbon storage in the SW Indian Ocean increased gradually until MIS 12 and 10, which show extreme glacial conditions. This gradual higher C storage capacity towards MIS 12 and 10 in the SW Indian Ocean was mainly controlled by progressively larger sea-ice cover related to 100-kyr eccentricity minima (Fig. 8b and 8d).

After MIS 10, a gradual transition from eccentricity- to obliquity-dominated cycles is observed for corrected benthic $\delta^{13}C$ in the spectral analyses (Fig. 7a and 7b), the wavelet power spectrum of corrected benthic $\delta^{13}C$ (Fig. 7c), and the power of the 100 and 41-kyr corrected benthic $\delta^{13}C$ cycles (Fig. 8a). As for the corrected benthic $\delta^{13}C$ record, the 100-kyr cycle of the $\delta^{18}O$ is less important than the 41-kyr obliquity cycle over the last 400 kyr (Fig. A.5b and A.5c). This replacement of 100-kyr eccentricity cycles by 41-kyr obliquity cycles, governing both sea-ice cover and related C storage changes (Fig. 8a), could be related to changes in the northern and southern hemispheres ice sheet dynamics (Starr et al., 2021). Before MIS 10, Southern Ocean climate was influenced by the complex non-linear 100-kyr response due to the northern hemisphere thick ice sheets established after the Mid-Pleistocene transition (Clark et al., 2006). Obliquity 41-kyr linear response of the Southern Ocean after MIS 10 might be caused by a stronger relationship between southern hemisphere ice sheets and obliquity (Zhang et al., 2013; Fogwill et al., 2015; Starr et al., 2021).

Our results highlight the importance of the SW Indian Ocean as a sink for CO_2 during glacial periods, when highest C storage occurred during relatively lower 100-kyr eccentricity and 41-kyr obliquity conditions, which fostered the largest sea-ice cover and lowest air-sea exchange of CO_2. In addition, our findings help to better constrain the dimensions of expanded glacial carbon-rich deep waters, which can increase the C storage capacity, with larger global volumes of southern-sourced nutrient-rich waters holding more CO_2 (Skinner, 2009).

6. Conclusions

We investigated the spatial and temporal evolution over the last 630 kyr of glacial carbon-rich deep waters entering the SW Indian based on foraminiferal ε_{Nd} and benthic $\delta^{13}C$ of two cores from the SW Indian Ocean.

Assuming that foraminiferal authigenic ε_{Nd} values essentially reflected the relative proportion between the northern- and the southern-sourced water whereas benthic $\delta^{13}C$ values varied with ventilation state, the comparison of ε_{Nd}-$\delta^{13}C$ relationship between the two cores revealed that glacial deep waters with a high accumulation of respired carbon bathed sites deeper than 2700 m. These southern-sourced deep waters could have extended at least until 33°S within the SW Indian Ocean.

Spatial and temporal expansion of glacial carbon-rich deep waters was governed by several forcing physical mechanisms. Periodicity analyses showed eccentricity (100 kyr) and obliquity (41 kyr) cycles in benthic $\delta^{13}C$ and $\delta^{18}O$ records from core MD96-2077, where the presence of glacial deep carbon rich waters was inferred. Furthermore, higher C storage occurred during glacial periods at times of relatively lower eccentricity and obliquity, showing an increasing trend in C storage from MIS 14 to MIS 10.

Acknowledgments

We thank the editor Dr Fabienne Marret-Davies for handling this manuscript. We are very thankful to two anonymous reviewers for their insightful comments that substantially improved this manuscript. JNPA was funded by the INDEXCLIMA project. This project has received funding from the European Union's Horizon 2020 research and innovation programme under the Marie Sklodowska-Curie grant agreement N°840675. Nd isotopic analyses were measured on Neptune+ MC-ICPMS acquired in the frame of EQUIPEX

ASTER-CEREGE project. We also thank the support of the INSU-LMC14 national laboratory for ARTEMIS radiocarbon dating for samples from core MD96-2052 and the INSU-LEFE-CLIMOZA project for stable isotope analyses from core MD96-2052. Marta Garcia for her technical support with ICP-MS Nd concentration measurements and Hélène Mariot for her careful maintenance of the clean laboratory are thanked. MiSo received support from the French National Programme LEFE (Les Enveloppes Fluides et l'Environnement) and from the French government under the France 2030 investment plan, as part of the Initiative d'Excellence d'Aix-Marseille Université - A*MIDEX (AMX-19-IET-012) and from the Research Federation ECCOREV (FR 3098; Aix-Marseille Univ., CNRS, INRAE, IRSN, CEA, Univ. Toulon, Univ. Avignon, Univ. Nimes).

Appendix A. Supplementary data

Supplementary figures A.1 to A.5

Appendix B. Supplementary data

Supplementary tables B.1 to B.4

Data availability

Data of this study can be found online in the supplemental files and in the database Pangaea (www.pangaea.de).

References

Adkins, J.F., 2013. The role of deep ocean circulation in setting glacial climates, Paleoceanography 28, 539–561, https://doi.org/10.1002/palo.20046

Amakawa, H., Yu, T.L., Tazoe, H., Obata, H., Gamo, T., Sano, Y., Shen, C.C., Suzuki, K., 2019. Neodymium concentration and isotopic composition distributions in the southwestern Indian Ocean and the Indian sector of the Southern Ocean. Chem. Geol. 511, 190–203. https://doi.org/10.1016/j.chemgeo.2019.01.007

Amsler, H.E., Thöle, L.M., Stimac, I., Geibert, W., Ikehara, M., Kuhn, G., Esper, O., Jaccard, S.L., 2022. Bottom water oxygenation changes in the southwestern Indian Ocean as an indicator for enhanced respired carbon storage since the last glacial inception. Clim. Past, 18, 1797–1813. https://doi.org/10.5194/cp-18-1797-2022

Bard, E., Rickaby, E.M., 2009. Migration of the subtropical front as a modulator of glacial climate. Nature 460, 380–383. https://doi.org/10.1038/nature08189

Bertrand, P., Shipboard Scientific Party, 1997. Les rapports de campagne à la mer à bord du Marion Dufresne - Campagne Nausicaa - IMAGES II - MD105 du 20/10/96 au 25/11/96. Institut Français pour la Recherche et la technologie Polaires.

Blaauw, M., Christen, J.A., 2011. Flexible paleoclimate age-depth models using an autoregressive gamma process. Bayesian Anal. 6, 457-474. https://doi.org/10.1214/11-BA618

[dataset] Boyer, Tim P.; Garcia, Hernan E.; Locarnini, Ricardo A.; Zweng, Melissa M.; Mishonov, Alexey V.; Reagan, James R.; Weathers, Katharine A.; Baranova, Olga K.; Seidov, Dan; Smolyar, Igor V., 2018. World Ocean Atlas 2018. NOAA National Centers for Environmental Information. https://www.ncei.noaa.gov/access/metadata/landing-page/bin/iso?id=gov.noaa.nodc:NCEI-WOA18

Carmack, E.C., Foster, T.D., 1975. On the flow of water out of the Weddell Sea. Deep Sea Research and Oceanographic Abstracts 22, 711–724. https://doi.org/10.1016/0011-7471(75)90077-7

Chadwick, M., Crosta, X., Esper, O., Thöle, L., Kohfeld, K. E., 2022. Compilation of Southern Ocean sea-ice records covering the last glacial-interglacial cycle (12–130 ka). Clim. Past 18, 1815–1829. https://doi.org/10.5194/cp-18-1815-2022

Charles, C., Pelleter, E., Révillon, S., Nonnote, P., Jorry, S.J., Kluska, J.M., 2020. Intermediate and deep ocean current circulation in the Mozambique Channel: new insights from ferromanganese crust Nd isotopes. Mar. Geol. 430, 106356. https://doi.org/10.1016/j.margeo.2020.106356

[dataset] Chen, M.-T., 1996. Planktic foraminifera (%) of sediment core MD96-2077. PANGAEA. https://doi.pangaea.de/10.1594/PANGAEA.66312Chen, M.-T., Bertrand, P., Balut, Y., Schneider, R., Rogers, J., Taiwan IMAGES Participants, 1998. IMAGES II cruise (NAUSICAA) explores Quaternary climatic variability and linkage of Benguela and Agulhas current systems in the southern Indian-Atlantic Ocean: participation by consortium of Taiwan institutions (coordinated by National Taiwan University). J. Geol. Soc. China 41, 73–80. http://wpes.gst.org.tw/cht/periodical_detial.php?s=70

Clark, P.U., Archer, D., Pollard, D., Blum, J.D., Rial, J.A., Brovkin, V., Mix, A.C., Pisias, N.G., Roy, M., 2006. The middle Pleistocene transition: characteristics, mechanisms, and implications for long-term changes in atmospheric pCO_2. Quat. Sci. Rev. 25, 3150–3184. https://doi.org/10.1016/j.quascirev.2006.07.008

Crosta, X., Kohfeld, K. E., Bostock, H. C., Chadwick, M., Du Vivier, A., Esper, O., Etourneau, J., Jones, J., Leventer, A., Müller, J., Rhodes, R. H., Allen, C. S., Ghadi, P., Lamping, N., Lange, C. B., Lawler, K.-A., Lund, D., Marzocchi, A., Meissner, K. J., Menviel, L., Nair, A., Patterson, M., Pike, J., Prebble, J. G., Riesselman, C., Sadatzki, H.,

Sime, L. C., Shukla, S. K., Thöle, L., Vorrath, M.-E., Xiao, W., Yang, J., 2022. Antarctic sea ice over the past 130 000 years – Part 1: a review of what proxy records tell us. Clim. Past 18, 1729–1756. https://doi.org/10.5194/cp-18-1729-2022

Curry, W.B., Oppo, D.W., 2005. Glacial water mass geometry and the distribution of $\delta^{13}C$ of ΣCO_2 in the western Atlantic Ocean, Paleoceanography, 20, PA1017, https://doi.org/10.1029/2004PA001021. https://doi.org/10.1029/2004PA001021

de Ruijter, W.P.M., Ridderinkhof, H., Lutjeharms, J.R.E., Schouten, M.W., Veth, C., 2002. Observations of the flow in the Mozambique Channel. Geophys. Res. Lett. 29, 140-1–140-3. https://doi.org/10.1029/2001GL013714

Ferrari, R., Jansen, M.F., Adkins, J.F., Burke, A., Stewart, A.L., Thompson, A.F., 2014. Antarctic Sea ice control on ocean circulation in present and glacial climates. Proc. Natl. Acad. Sci. U. S. A. 111 (24), 8753–8758. https://doi.org/10.1073/pnas.1323922111

Fogwill, C.J., Turney, C.S.M., Hutchinson, D.K., Taschetto, A.S., England, M.H., 2015. Obliquity control on southern hemisphere climate during the last glacial. Sci. Rep. 5, 11673. https://doi.org/10.1038/srep11673

Gebbie, G., 2014. How much did glacial North Atlantic water shoal? Paleoceanography 29, 190–209. https://doi.org/10.1002/2013PA002557

Goldstein, S., Hemming, S.R., 2003. Long-lived Isotopic Tracers in Oceanography, Paleoceanography, and Ice-sheet Dynamics, in: H.D. Holland and K.K. Turekian (Eds.), Treatise on Geochemistry Volume 6: The oceans and Marine Geochemistry. Elsevier Pergamon press, pp. 453–489. https://doi.org/10.1016/B0-08-043751-6/06179-X

Hain, M.P., Sigman, D.M., Haug, G.H., 2010. Carbon dioxide effects of Antarctic stratification, North Atlantic Intermediate Water formation, and subantarctic nutrient drawdown during the last ice age: diagnosis and synthesis in a geochemical box model. Global Biogeochem. Cycles 24, GB4032. https://doi.org/10.1029/2010GB003790

Hammer, Ø., Harper, D.A.T., Ryan, P.D., 2001. PAST: Paleontological Statistics software package for education and data analysis. Palaeontol. Elec. 4, Article 4. https://palaeo-electronica.org/2001_1/past/issue1_01.htm

Hasenfratz, A.P., Jaccard, S.L., Martínez-García, A., Sigman, D.M., Hodell, D.A., Vance, D., Bernasconi, S.M., Kleiven, H.F., Haumann, F.A., Haug, G.H., 2019. The residence time of Southern Ocean surface waters and the 100,000-year ice age cycle. Science 363, 1080–1084. https://doi.org/10.1126/science.aat7067

Hays, J.D., Imbrie, J., Shackleton, N.J., 1976. Variations in the Earth's Orbit: Pacemaker of the Ice Age. Science 194, 1121–1132. https://doi.org/10.1126/science.194.4270.1121

Heaton, T.J., Köhler, P., Butzin, M., Bard, E., Reimer, R.W., Austin, W.E.N., Bronk Ramsey, C., Grootes, P.M., Hughen, K.A., Kromer, B., Reimer, P.J., Adkins, J., Burke, A., Cook, M.S., Olsen, J., Skinner, L.C., 2020. Marine20-the marine radiocarbon age calibration curve (0-55,000 cal BP). Radiocarbon 62, 779–820. https://doi.org/10.1017/RDC.2020.68

Hines, S.K.V., Bolge, L., Goldstein, S.L., Charles, C.D., Hall, I.R., Hemming, S.R., 2021. Little change in ice age water mass structure from Cape Basin benthic neodymium and carbon isotopes. Paleoceanogr. Paleoclimatol. 36, e2021PA004281. https://doi.org/10.1029/2021PA004281

Hodell, D.A., Charles, C.D., Curtis, J.H., Mortyn, P.G., Ninnemann, U.S., Venz, K.A., 2003. Data report: Oxygen isotope stratigraphy of ODP Leg 177 Sites 1088, 1089, 1090, 1093, and 1094, in: Gersonde, R., Hodell, D.A., Blum, P. (Eds.), Proc. ODP, Sci. Results, 177, pp. 1–26. https://doi:10.2973/odp.proc.sr.177.120.2003

Hoogakker, B.A.A., Rohling, E.J., Palmer, M.R., Tyrrell, T., Rothwell, R.G., 2006. Underlying causes for long-term global ocean d13C fluctuations over the last 1.20 Myr. Earth Planet. Sci. Lett. 248, 15–29. https://doi.org/10.1016/j.epsl.2006.05.007

Howe, J.N.W., Piotrowski, A.M., Noble, T.L., Mulitza, S., Chiessi, C.M., Bayon, G., 2016. North Atlantic deep water production during the last glacial Maximum. Nat. Commun. 7, 11765. https://doi.org/10.1038/ncomms11765

Huang, H., Gutjahr, M., Eisenhauer, A., Kuhn, G., 2020. No detectable Weddell Sea Antarctic Bottom Water export during the Last and Penultimate Glacial Maximum. Nature Communications 11, 424, https://doi.org/10.1038/s41467-020-14302-3

Key, R.M., Kozyr, A., Sabine, C.L., Lee, K., Wanninkhof, R., Bullister, J.L., Feely, R.A., Millero, F.J., Mordy, C., Peng, T.H., 2004. A global ocean carbon climatology: results from global data analysis project (GLODAP). Global Biogeochem. Cycles 18, GB4031. https://doi.org/10.1029/2004GB002247

Kuhlbrodt, T., Griesel, A., Montoya, M., Levermann, A., Hofmann, M., Rahmstorf, S., 2007. On the driving processes of the Atlantic meridional overturning circulation. Rev. Geophys. 45, RG2001. https://doi.org/10.1029/2004RG000166

Lancelot, Y., Shipboard Scientific Party, 1997. Les rapports de campagne à la mer à bord du Marion Dufresne - Campagne MOZAPHARE-MD104 du 17/07/96 au 08/08/96. Institut Français pour la Recherche et la technologie Polaires.

Larqué, L., Maamaatuaiahutapu, K., Garçon, V., 1997. On the intermediate and deep water flows in the South Atlantic Ocean. J. Geophys. Res.: Oceans 102, 12425–12440. https://doi.org/10.1029/97JC00629

Lathika, N., Rahaman, W., Tarique, M., Gandhi, N., Kumar, A., Thamban, M., 2021. Deep water circulation in the Arabian Sea during the last glacial cycle: Implications for paleo-redox condition, carbon sink and atmospheric CO_2 variability. Quat. Sci. Rev. 257, 106853. https://doi.org/10.1016/j.quascirev.2021.106853

Lear, C.H., Billups, K., Rickaby, R.E.M., Diester-Haass, L., Mawbey, E.M., Sosdian, S.M., 2016. Breathing more deeply: deep ocean carbon storage during the mid-Pleistocene climate transition. Geology 44, 1035–1038. https://doi.org/10.1130/G38636.1

Lhardy, F., Bouttes, N., Roche, D.M., Abe-Ouchi, A., Chase, Z., Crichton, K.A., Ilyina, T. Ivanovic, R. Jochum, M., Kageyama, M., Kobayashi, H., Liu, B., Menviel, L., Muglia, J., Nuterman, R., Oka, A., Vettoretti, G., Yamamoto, A., 2021. A first intercomparison of the simulated LGM carbon results within PMIP-carbon: Role of the ocean boundary conditions. Paleoceanogr. Paleoclimat. 36, e2021PA004302. https://doi. org/10.1029/2021PA004302

Lisiecki, L.E., Raymo, M.E., 2005. A Pliocene-Pleistocene stack of 57 globally distributed benthic $\delta^{18}O$ records. Paleoceanography 20, 1–17. https://doi.org/10.1029/2004PA001071

Marchant, R., Tetard, M., Pratiwi, A., Adebayo, M., de Garidel-Thoron, T., 2020. Automated analysis of foraminifera fossil records by image classification using a convolutional neural network. J. Micropalaeontol. 39, 183–202. https://doi.org/10.5194/jm-39-183-2020

Marzocchi, A., Jansen, M.F., 2019. Global cooling linked to increased glacial carbon storage via changes in Antarctic sea ice. Nat. Geosci. 12, 1001–1005. https://doi.org/10.1038/s41561-019-0466-8

Mix, A.C., Fairbanks, R.G., 1985. North Atlantic surface-ocean control of Pleistocene deep-ocean circulation. Earth Planet. Sci. Lett. 73, 231–243. https://doi.org/10.1016/0012-821X(85)90072-X

Mix, A.C., Le, J., Shackleton, N.J., 1995. Benthic foraminifer stable isotope stratigraphy of Site 846: 0–1.8 Ma, in: Pisias, N.G., Mayer, L., Janecek, T., Palmer-Julson, A., van Andel, T.H. (Eds.), Proceedings of the ODP, Scientific Results, vol. 138. Ocean Drilling Program, College Station, TX, pp. 839–856. https://doi.org/10.2973/odp.proc.sr.138.160.1995

Orsi, A. H., Johnson, G. C., Bullister, J. L., 1999. Circulation, mixing, and production of Antarctic Bottom Water. Prog. Oceanogr. 43, 55-109. https://doi.org/10.1016/S0079-6611(99)00004-X.

Pena, L.D., Goldstein, S.L., 2014. Thermohaline circulation crisis and impacts during the mid-Pleistocene transition. Science 345, 318–322. https://doi.org/10.1126/science.1249770

Peterson, C.D., Lisiecki, L.E., Stern, J.V., 2014. Deglacial whole-ocean $\delta^{13}C$ change estimated from 480 benthic foraminiferal records. Paleoceanography 29, 549–563. https://doi.org/10.1002/2013PA002552

Pichon, J.J., Labeyrie, L.D., Bareille, G., Labracherie, M., Duprat, J., Jouzel, J., 1992. Surface water temperature changes in the high latitudes of the Southern Hemisphere over the last Glacial-Interglacial cycle. Paleoceanography 7, 289–318. https://doi. org/10.1029/92PA00709

Pin, C., Santos Zalduegui, J.F., 1997. Sequential separation of light rare-earth elements, thorium and uranium by miniaturized extraction chromatography: application to isotopic analyses of silicate rocks. Anal. Chim. Acta 339, 79–89. https://doi.org/10.1016/S0003-2670(96)00499-0

Piotrowski, A.M., Banakar, V.K., Scrivner, A.E., Elderfield, H., Galy, A., Dennis, A., 2009. Indian Ocean circulation and productivity during the last glacial cycle. Earth Planet. Sci. Lett. 285, 179–189. https://doi.org/10.1016/j.epsl.2009.06.007.

Robinson, S., Ivanovic, R., van de Flierdt, T., Blanchet, C.L., Tachikawa, K., Martin, E.E., Cook, C.P., Williams, T., Gregoire, L., Plancherel, Y., Jeandel, C., Arsouze, T., 2021. Global continental and marine detrital ε_{Nd}: An updated compilation for use in understanding marine Nd cycling. Chem. Geol. 567, 120119, https://doi.org/10.1016/j.chemgeo.2021.120119.

Sarmiento, J., Toggweiler, J., 1984. A new model for the role of the oceans in determining atmospheric PCO_2. Nature 308, 621–624. https://doi.org/10.1038/308621a0

Schlitzer, R., 2015. Ocean Data View.

Schmittner, A., Gruber, N., Mix, A.C., Key, R.M., Tagliabue, A., Westberry, T.K., 2013. Biology and air–sea gas exchange controls on the distribution of carbon isotope ratios ($\delta^{13}C$) in the ocean. Biogeosciences 10, 5793–5816. https://doi.org/10.5194/bg-10-5793-2013.

Shackleton, N.J., 2000. The 100,000-year ice-age cycle identified and found to lag temperature, carbon dioxide, and orbital eccentricity. Science 289, 1897–1902. https://doi.org/10.1126/science.289.5486.1897

Sigman, D., Boyle, E., 2000. Glacial/interglacial variations in atmospheric carbon dioxide. Nature 407, 859–869. https://doi.org/10.1038/35038000

Sigman, D., Hain, M., Haug, G., 2010. The polar ocean and glacial cycles in atmospheric CO_2 concentration. Nature 466, 47–55. https://doi.org/10.1038/nature09149

Sigman, D.M., Fripiat, F., Studer, A.S., Kemeny, P.C., Martínez-García, A., Hain, M.P., Ai, X., Wang, X., Ren, H., Haug, G.H., 2021. The Southern Ocean during the ice ages: a review of the Antarctic surface isolation hypothesis, with comparison to the North Pacific. Quat. Sci. Rev. 254, 106732. https://doi.org/10.1016/j.quascirev.2020.106732

Skinner, L.C., 2009. Glacial-interglacial atmospheric CO2 change: a possible "standing volume" effect on deep-ocean carbon sequestration. Clim. Past 5, 537–550. https://doi.org/10.5194/cp-5-537-2009

Starr, A., Hall, I.R., Barker, S., Rackow, T., Zhang, X., Hemming, S.R., van der Lubbe, H.J.L., Knorr, G., Berke, M.A., Bigg, G.R., Cartagena-Sierra, A., Jiménez-Espejo, F.J., Gong, X., Gruetzner, J., Lathika, N., LeVay, L.J., Robinson, R.S., Ziegler, M., Expedition

361 Science Party, 2021. Antarctic icebergs reorganize ocean circulation during Pleistocene glacials. Nature 589, 236–241. https://doi.org/10.1038/s41586-020-03094-7

Stein, K., Timmermann, A., Kwon, E.Y., Friedrich, T., 2020. Timing and magnitude of Southern Ocean sea ice/carbon cycle feedbacks. Proc. Natl. Acad. Sci. USA117, 4498–4504. https://doi.org/10.1073/pnas.1908670117

Stephens, B., Keeling, R., 2000. The influence of Antarctic sea ice on glacial–interglacial CO_2 variations. Nature 404, 171–174. https://doi.org/10.1038/35004556

Tachikawa, K., Piotrowski, A.M., Bayon, G., 2014. Neodymium associated with foraminiferal carbonate as a recorder of seawater isotopic signatures. Quat. Sci. Rev. 88, 1–13. https://doi.org/10.1016/j.quascirev.2013.12.027

Tachikawa, K., Arsouze, T., Bayon, G., Bory, A., Colin, C., Dutay, J. -C., Frank, N., Giraud, X., Gourlan, A.T., Jeandel, C., Lacan, F., Meynadier, L., Montagna, P., Piotrowski, A.M., Plancherel, Y., Pucéat, E., Roy-Barman, M., Waelbroeck, C., 2017. The large-scale evolution of neodymium isotopic composition in the global modern and Holocene ocean revealed from seawater and archive data. Chem. Geol. 457, 131–148. https://doi.org/10.1016/j.chemgeo.2017.03.018

Tachikawa, K., Rapuc, W., Vidal, L., Dubois-Dauphin, Q., Westerhold, T., Guihou, A., Bickert, T., Pérez-Asensio, J.N., Deschamps, P., Skonieczny, C., 2021. Eastern Atlantic deep-water circulation and carbon storage inferred from neodymium and carbon isotopic compositions over the past 1.1 million years. Quaternary Sci. Rev. 252, 106752. https://doi.org/10.1016/j.quascirev.2020.106752

Talley, L.D., 2013. Closure of the global overturning circulation through the Indian, pacific, and southern oceans: schematics and transports. Oceanography 26, 80–97. https://doi.org/10.5670/oceanog.2013.07

Tanaka, T., Togashi, S., Kamioka, H., Amakawa, H., Kagami, H., Hamamoto, T., Yuhara, M., Orihashi, Y., Yoneda, S., Shimizu, H., Kunimaru, T., Takahashi, K., Yanagi, T., Nakano, T., Fujimaki, H., Shinjo, R., Asahara, Y., Tanimizu, M., Dragusanu, C., 2000. JNdi-1: a neodymium isotopic reference in consistency with LaJolla neodymium. Chem. Geol. 168, 279–281. https://doi.org/10.1016/S0009-2541(00)00198-4

Toggweiler, J.R., Russell, J.L., Carson S.R., 2006. Midlatitude westerlies, atmospheric CO_2, and climate change during the ice ages, Paleoceanography, 21, PA2005, doi:10.1029/2005PA001154

Tomczak, M., Godfrey, J.S., 1994. The Indian Ocean, in: Tomczak, M., Godfrey, J.S. (Eds.), Regional Oceanography: An Introduction. Pergamon, England, pp. 193–220. https://doi.org/10.1016/B978-0-08-041021-0.50015-1

Wilson, D.J., Piotrowski, A.M., Galy, A., McCave, I.N., 2012. A boundary exchange influence on deglacial neodymium isotope records from the deep western Indian Ocean. Earth Planet. Sci. Lett. 341–344, 35–47. http://dx.doi.org/10.1016/j.epsl.2012.06.009

Yu, J., Menviel, L., Jin, Z.D., Anderson, R.F., Jian, Z., Piotrowski, A.M., Ma, X., Rohling, E.J., Zhang, F., Marino, G., McManus, J.F., 2020. Last glacial atmospheric CO_2 decline due to widespread Pacific deep-water expansion. Nat. Geosci. 13, 628–633. https://doi.org/10.1038/s41561-020-0610-5

Zhang, X., Lohmann, G., Knorr, G., Xu, X., 2013. Different ocean states and transient characteristics in Last Glacial Maximum simulations and implications for deglaciation. Clim. Past 9, 2319–2333. https://doi.org/10.5194/cp-9-2319-2013

Zhang, H., Luo, Y., Yu, J., Zhang, L., Xiang, R., Yu, Z., Huang, H., 2022. Indian Ocean sedimentary calcium carbonate distribution and its implications for the glacial deep ocean circulation. Quat. Sci. Rev. 284, 107490. https://doi.org/10.1016/j.quascirev.2022.107490.

Ziegler, M., Diz, P., Hall, I.R., Zahn, R., 2013. Millennial-scale changes in atmospheric CO_2 levels linked to the Southern Ocean carbon isotope gradient and dust flux. Nat. Geosci. 6, 457–461. https://doi.org/10.1038/ngeo1782

Figures captions

Figure 1. a) Simplified modern ocean circulation of the study area with the core locations of this study (black stars): MD96-2077 (33°10.1'S, 31°14.8'E, 3781 m water depth), and core MD96-2052 (19°52.7'S, 41°49.9'E, 2627 m water depth); and previous studies cores (white dots): core MD02-2588/Agulhas Plateau (AP) composite (41°19.9'S, 25°49.7'E, 2907 m water depth) (Ziegler et al., 2013; Starr et al., 2021), core MD84-527 (43°49'3S, 51°19'1E, 3262 m water depth) (Pichon et al., 1992), core ODP1090 (42°54.82'S, 8°53.98'E, 3702 m water depth) (Hodell et al., 2003) and core SK129–CR2 (3°N, 76°E, 3800 m water depth) (Piotrowski et al., 2009). The colored arrows depict modern flow paths of different water masses: North Atlantic Deep Water (NADW, blue), Circumpolar Deep Water (CDW, purple), and Antarctic Bottom Water (AABW, dark brown). b) SW-NE salinity transect along latitude showing the major water masses: NADW, CDW, AAIW (Antarctic Intermediate Water), NIDW (North Indian Deep Water) and surface water. Symbols as for a). Figures are created with the software Ocean Data View (ODV) (Schlitzer, 2015). (For interpretation of the references to color in this figure legend, the reader is referred to the web version of this article.)

Figure 2. Potential temperature and salinity diagram of the modern southeastern Atlantic and southwest Indian waters based on Electronic Atlas of WOA Data at cores MD96-2077, MD96-2052 and ODP1090. The grey squares indicate the source water type Potential temperature and salinity for NADW, Upper Circumpolar Deep Water (UCDW) and Lower

Circumpolar Deep Water (LCDW) (Larqué et al., 1997). AABW with a negative temperature is not shown in this diagram. (For interpretation of the references to color in this figure legend, the reader is referred to the web version of this article.)

Figure 3. a) Benthic foraminiferal $\delta^{18}O$ of MD96-2052 (orange) and MD96-2077 (blue). b) foraminiferal ε_{Nd} of MD96-2052 (orange) and MD96-2077 (blue), modern NADW seawater ε_{Nd} (dark brown) and estimated seawater ε_{Nd} at core sites MD96-2052 (red) and MD96-2077 (sky blue). c) benthic foraminiferal $\delta^{13}C$ of MD96-2052 (orange) and MD96-2077 (blue). (For interpretation of the references to color in this figure legend, the reader is referred to the web version of this article.)

Figure 4. a) Relationship between benthic $\delta^{13}C$ and foraminiferal ε_{Nd} of MD96-2052 (orange) (this study), MD96-2077 (blue) (this study), ODP1090 (purple) (Hodell et al., 2003; Pena and Goldstein, 2014), and SK129–CR2 (grass green) (Piotrowski et al., 2009). Data influenced by organic fluxes or cold climate substages are colored in light blue. Open symbols are used for glacial periods and closed symbols for interglacial periods. Terminations' data are indicated with stars. The upper black line is the binary mixing line defined by the present-day NADW and CDW endmembers: for NADW, ε_{Nd} -12.3 ± 0.9 (1σ), dissolved Nd concentration = 20.3 ± 3.2 (1σ) pmol/kg, $\delta^{13}C$-DIC = 1.1 ± 0.3‰ (uncertainty is arbitrarily fixed to be 0.3‰) and DIC concentration = 2175 ± 109 mmol/kg (uncertainty is arbitrarily fixed to be 5%), for CDW ε_{Nd} -7.8 ± 1.2 (1σ), dissolved Nd concentration = 24.0 ± 4.8 (1s) pmol/kg, $\delta^{13}C$-DIC = 0.4 ± 0.3‰ (uncertainty is arbitrarily fixed to be 0.3‰) and DIC concentration = 2285 ± 114 mmol/kg (uncertainty is arbitrarily fixed to be 5%). The ε_{Nd} and Nd concentration values are derived from Tachikawa et al. (2017). The $\delta^{13}C$-DIC and the DIC concentration values are obtained from Schmittner et al. (2013) and Key et al. (2004), respectively. The glacial binary

mixing line between Glacial North Atlantic Intermediate Water (GNAIW) and Glacial Pacific Deep Water (GPDW), and the Glacial Antarctic Bottom Water (GAABW) endmember value are based on published values from Yu et al. (2020). Red crosses indicate A-F periods from figure 8. (For interpretation of the references to color in this figure legend, the reader is referred to the web version of this article.)

Figure 5. Benthic foraminiferal $\delta^{13}C$ of cores MD96-2052 (orange) (this study), AP composite (gold) (Ziegler et al., 2013; Starr et al., 2021), MD84-527 (pink) (Pichon et al., 1992), and MD96-2077 (blue) (this study), compared with the global stacked benthic $\delta^{13}C$ record (black) (Hoogakker et al., 2006). (For interpretation of the references to color in this figure legend, the reader is referred to the web version of this article.)

Figure 6. Map showing the possible extension of glacial depleted $\delta^{13}C$ deep water masses (>2700 m) into the SW Indian Ocean (dash purple line). A doubtful pathway is indicated by the dash purple arrow. Black stars represent studied cores and white dots previous studies cores. (For interpretation of the references to color in this figure legend, the reader is referred to the web version of this article.)

Figure 7. a) Power spectrum of the corrected benthic $\delta^{13}C$ of core MD96-2077 (last 630 kyr) with principal orbital periodicities indicated in kiloyears. The 90% confidence interval (CI) is shown. b) Power spectrum of the corrected benthic $\delta^{13}C$ of core MD96-2077 (last 400 kyr) with major orbital periodicities indicated in kiloyears. The 90% confidence interval (CI) is depicted. c) wavelet power spectrum of the corrected benthic $\delta^{13}C$ of core MD96-2077 (last 630 kyr). Main orbital cycles are marked with dash lines. (For interpretation of the references to color in this figure legend, the reader is referred to the web version of this article.)

Figure 8. a) Power of the corrected benthic $\delta^{13}C$ of core MD96-2077 in the 100-kyr eccentricity (purple) and 41-kyr obliquity (magenta) frequency bands. b) 100-kyr filtered corrected benthic $\delta^{13}C$ of core MD-96-2077 (purple) and filtered 100-kyr eccentricity (black). c) 41-kyr filtered corrected benthic $\delta^{13}C$ of core MD-96-2077 (magenta) and filtered 41-kyr obliquity (black). d) Corrected benthic $\delta^{13}C$ of core MD-96-2077 (blue) (this study), diatom *Fragilariopsis curta* and *F. cylindrus* relative abundances of core SK200/33 (red brown) (Chadwick et al., 2022) and IRD_{MAR} (cm^2/kyr) of AP composite site (forest green) (Starr et al., 2021). Red rectangles show periods (A-F) of more depleted corrected benthic $\delta^{13}C$ of core MD-96-2077 (higher carbon storage) at times of low eccentricity and obliquity. (For interpretation of the references to color in this figure legend, the reader is referred to the web version of this article.)

Declaration of interests

☒The authors declare that they have no known competing financial interests or personal relationships that could have appeared to influence the work reported in this paper.

☐The authors declare the following financial interests/personal relationships which may be considered as potential competing interests:

- Analysis of authigenic ε_{Nd} and benthic $\delta^{13}C$ were combined for the last 630 kyr.
- Glacial C-rich deep waters were present below 2700 m extending into the SW Indian.
- Glacial carbon storage increased during low eccentricity and obliquity.
- C storage changed gradually from 100-kyr eccentricity to 41-kyr obliquity cycles.

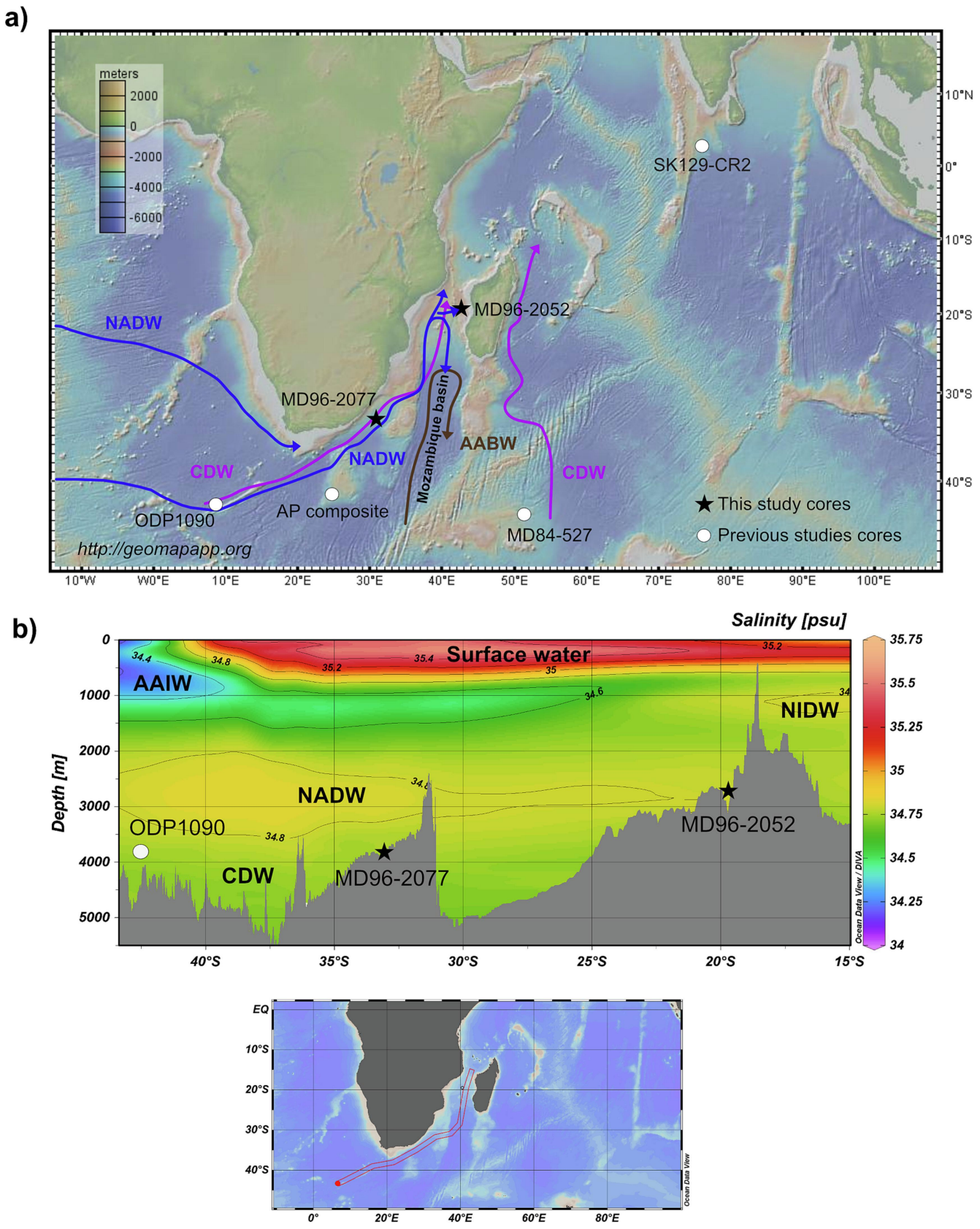
a)
meters
2000
0
-2000
-4000
-6000
SK129-CR2
MD96-2052
NADW
MD96-2077
Mozambique basin
AABW
NADW
CDW
CDW
ODP1090
AP composite
MD84-527
This study cores
Previous studies cores
http://geomapapp.org
10°N
0°
10°S
20°S
30°S
40°S
10°W
W0°E
10°E
20°E
30°E
40°E
50°E
60°E
70°E
80°E
90°E
100°E
b)
Salinity [psu]
Depth [m]
Surface water
AAIW
NIDW
NADW
CDW
ODP1090
MD96-2077
MD96-2052
Ocean Data View / DIVA
40°S
35°S
30°S
25°S
20°S
15°S
EQ
10°S
20°S
30°S
40°S
0°
20°E
40°E
60°E
80°E
Ocean Data View

Figure 1

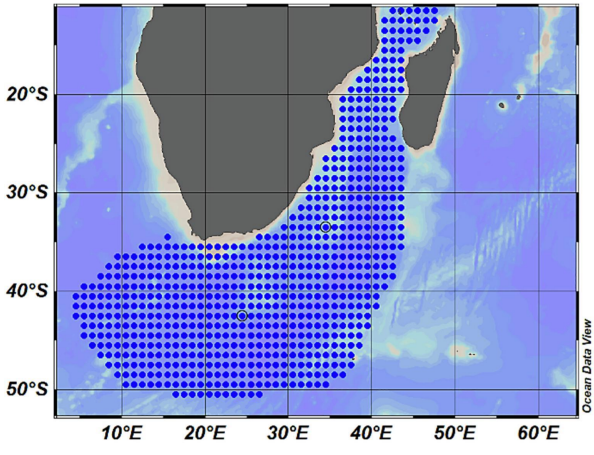
20°S
30°S
40°S
50°S
10°E
20°E
30°E
40°E
50°E
60°E
Ocean Data View

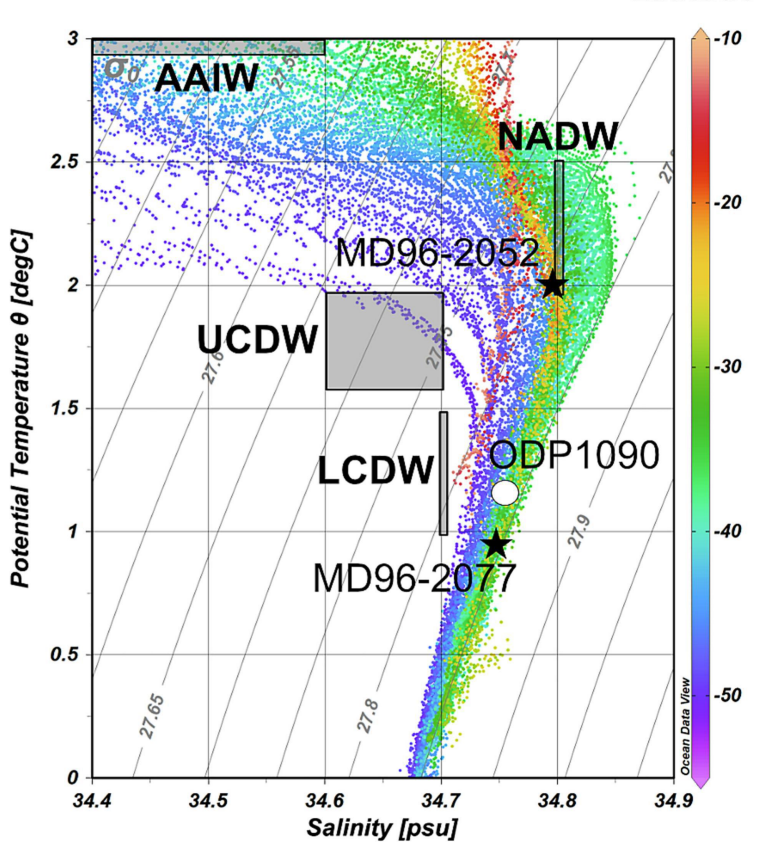
Latitude
AAIW
NADW
MD96-2052
UCDW
LCDW
ODP1090
MD96-2077
Potential Temperature θ [degC]
Salinity [psu]
27.65
27.8
27.9
Ocean Data View

Figure 2

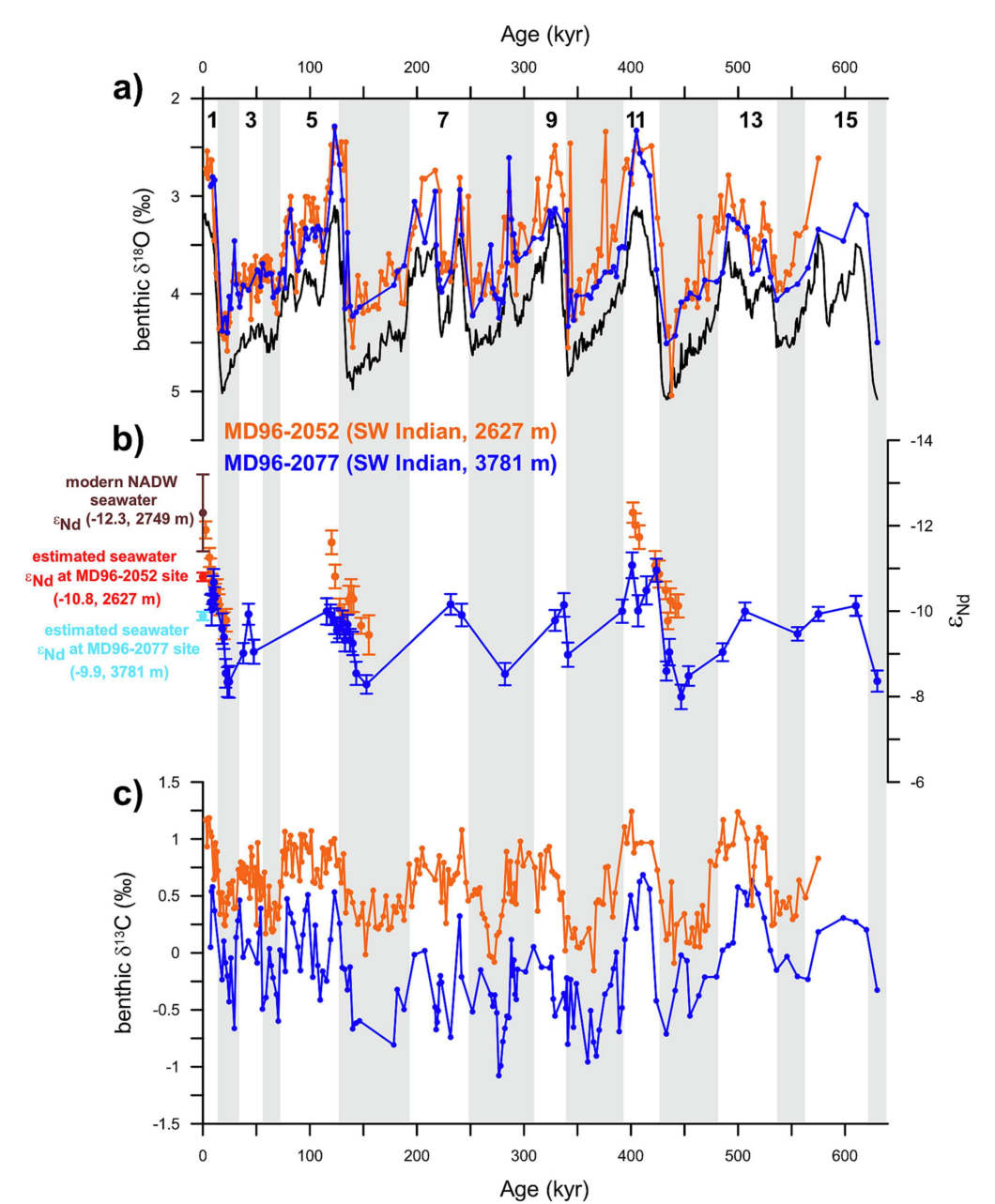
Age (kyr)
a)
benthic δ18O (‰)
1
3
5
7
9
11
13
15
b)
MD96-2052 (SW Indian, 2627 m)
MD96-2077 (SW Indian, 3781 m)
modern NADW seawater εNd (-12.3, 2749 m)
estimated seawater εNd at MD96-2052 site (-10.8, 2627 m)
estimated seawater εNd at MD96-2077 site (-9.9, 3781 m)
εNd
c)
benthic δ13C (‰)
Age (kyr)

Figure 3

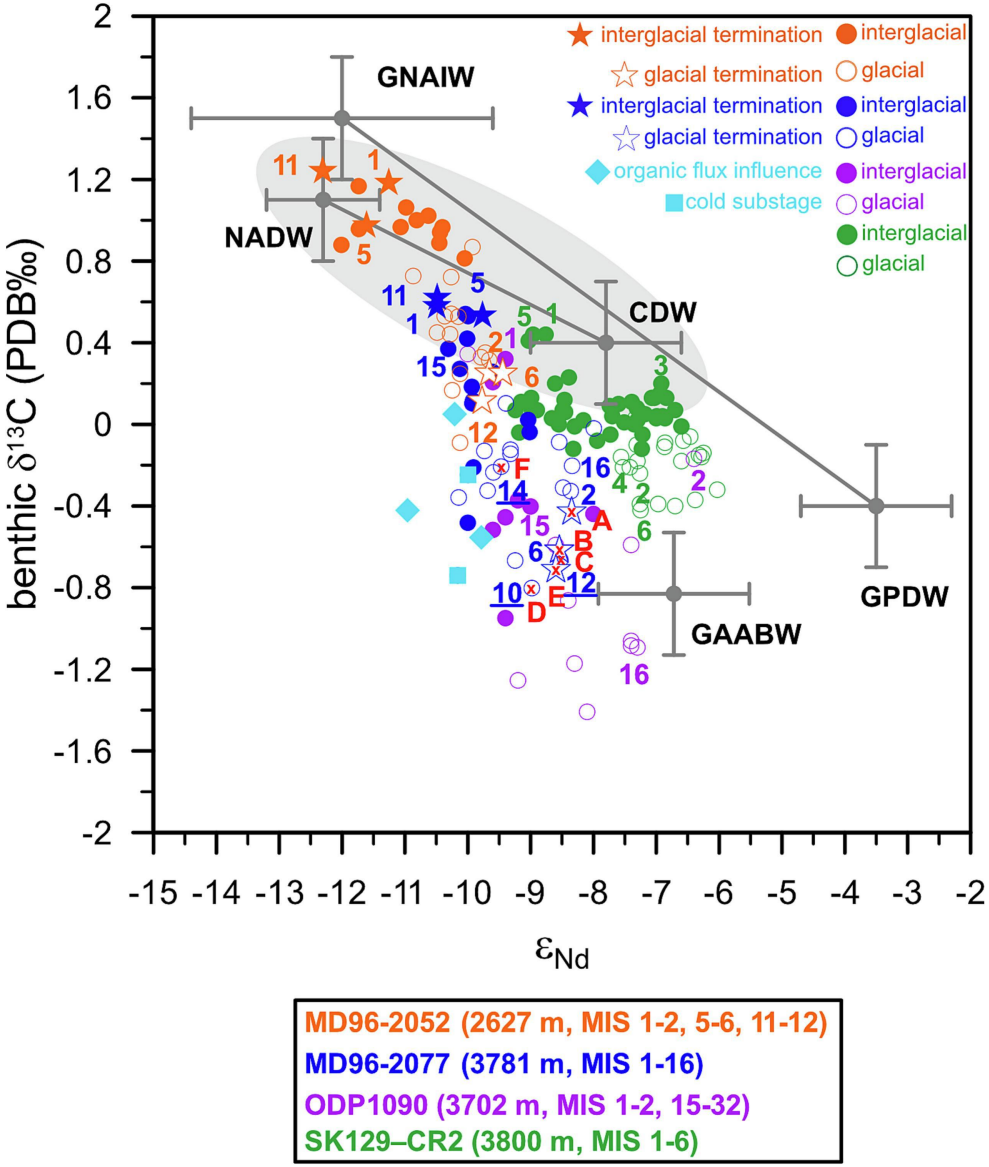
interglacial termination
glacial termination
interglacial termination
glacial termination
organic flux influence
cold substage
interglacial
glacial
interglacial
glacial
interglacial
glacial
GNAIW
NADW
CDW
GPDW
GAABW
benthic δ13C (PDB‰)
εNd
2
1.6
1.2
0.8
0.4
0
-0.4
-0.8
-1.2
-1.6
-2
-15 -14 -13 -12 -11 -10 -9 -8 -7 -6 -5 -4 -3 -2
MD96-2052 (2627 m, MIS 1-2, 5-6, 11-12)
MD96-2077 (3781 m, MIS 1-16)
ODP1090 (3702 m, MIS 1-2, 15-32)
SK129–CR2 (3800 m, MIS 1-6)

Figure 4

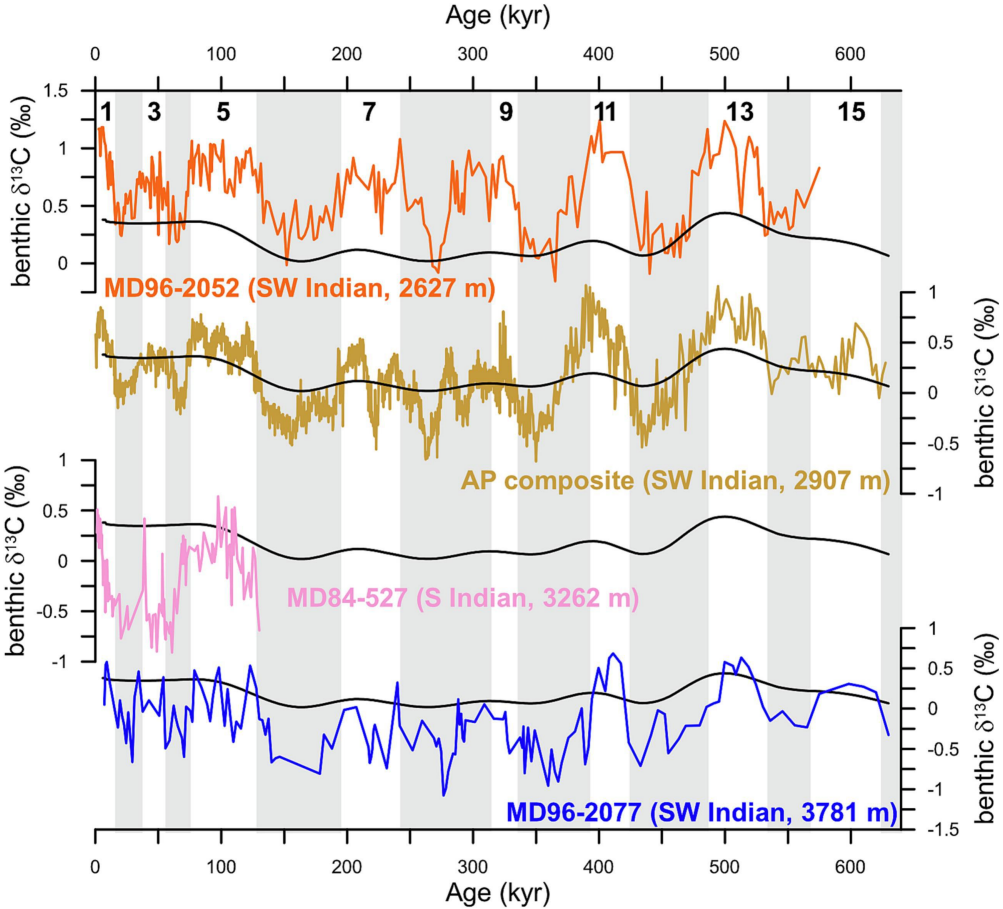
Age (kyr)
0
100
200
300
400
500
600
1
3
5
7
9
11
13
15
benthic δ13C (‰)
1.5
1
0.5
0
MD96-2052 (SW Indian, 2627 m)
AP composite (SW Indian, 2907 m)
-0.5
-1
MD84-527 (S Indian, 3262 m)
-1.5
MD96-2077 (SW Indian, 3781 m)

Figure 5

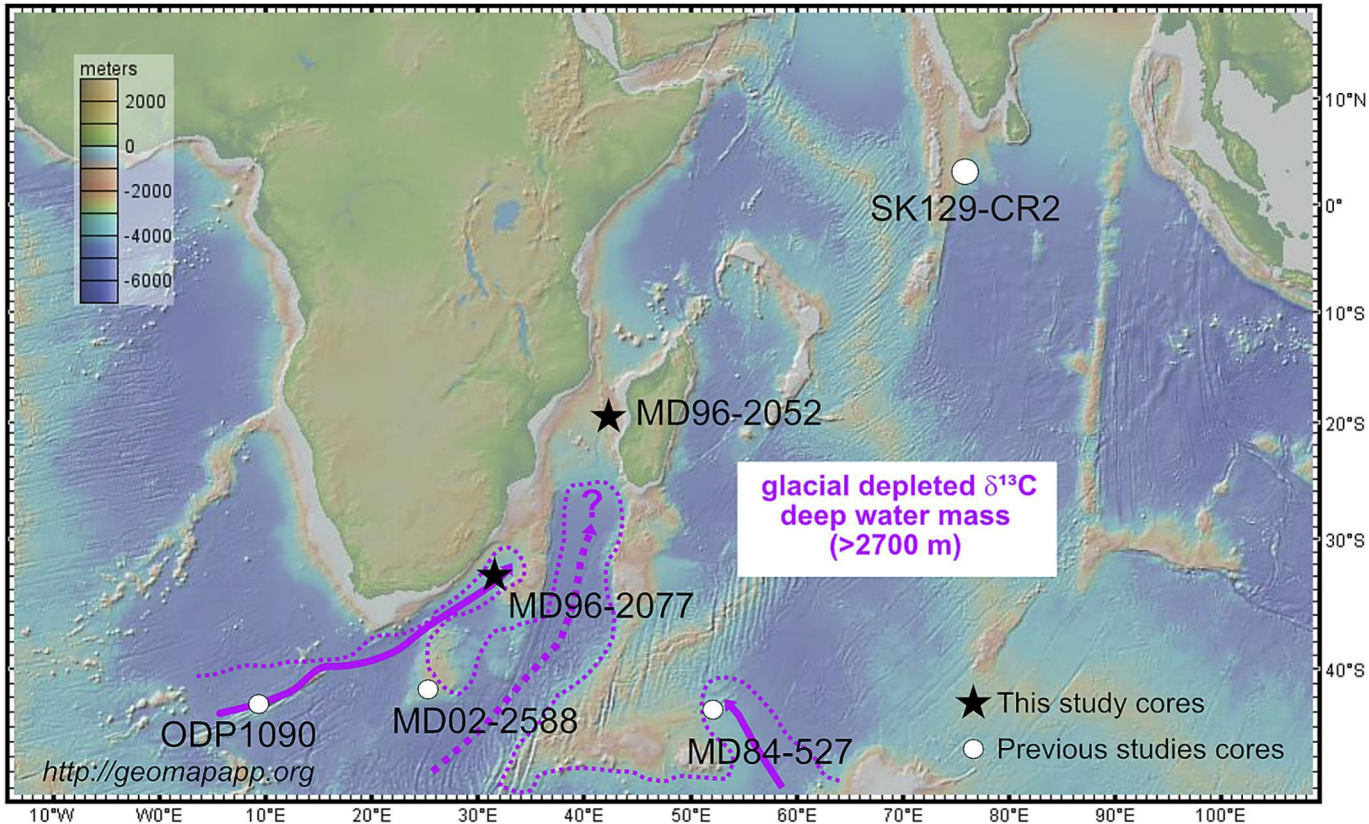
meters
2000
0
-2000
-4000
-6000
SK129-CR2
MD96-2052
glacial depleted δ13C
deep water mass
(>2700 m)
?
MD96-2077
ODP1090
MD02-2588
MD84-527
This study cores
Previous studies cores
http://geomapapp.org
10°N
0°
10°S
20°S
30°S
40°S
10°W
W0°E
10°E
20°E
30°E
40°E
50°E
60°E
70°E
80°E
90°E
100°E

Figure 6

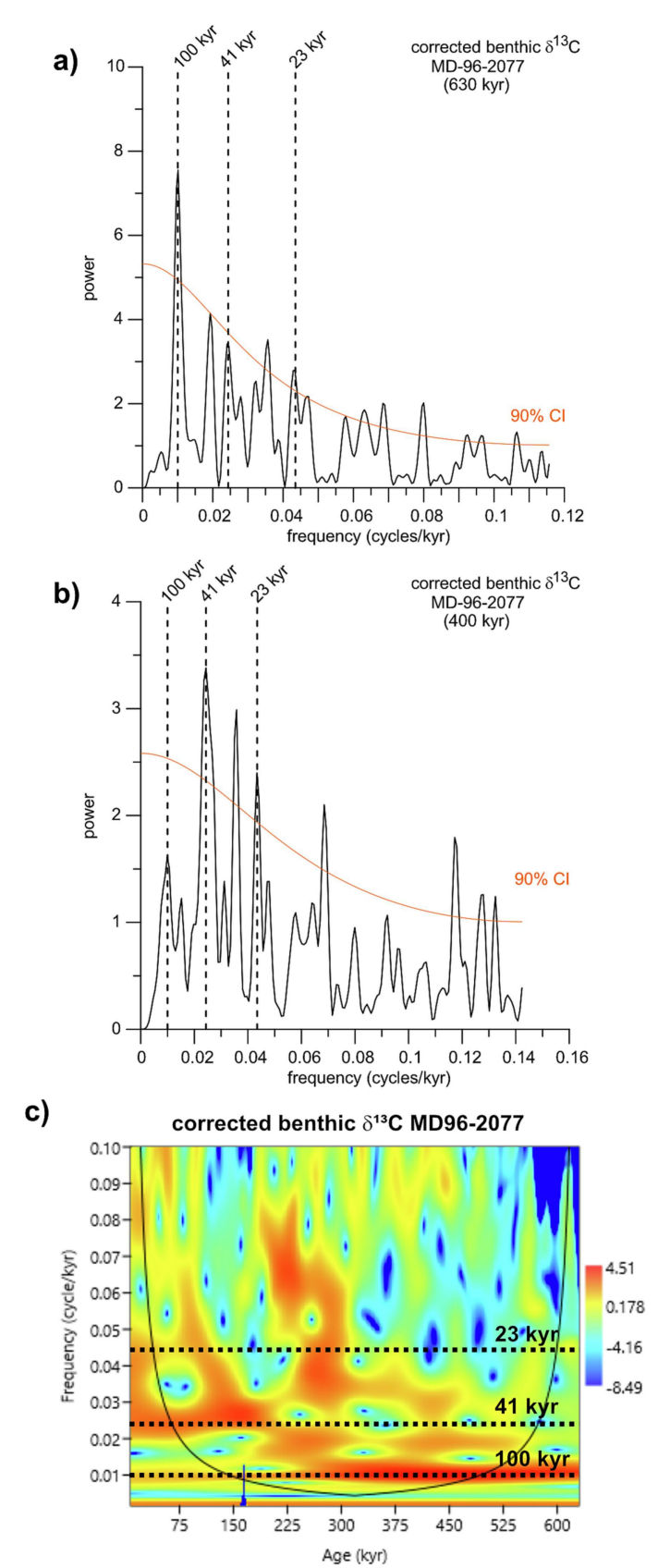
a)
100 kyr
41 kyr
23 kyr
corrected benthic δ13C
MD-96-2077
(630 kyr)
power
90% CI
frequency (cycles/kyr)
b)
100 kyr
41 kyr
23 kyr
corrected benthic δ13C
MD-96-2077
(400 kyr)
power
90% CI
frequency (cycles/kyr)
c)
corrected benthic δ13C MD96-2077
Frequency (cycle/kyr)
23 kyr
41 kyr
100 kyr
4.51
0.178
-4.16
-8.49
Age (kyr)

Figure 7

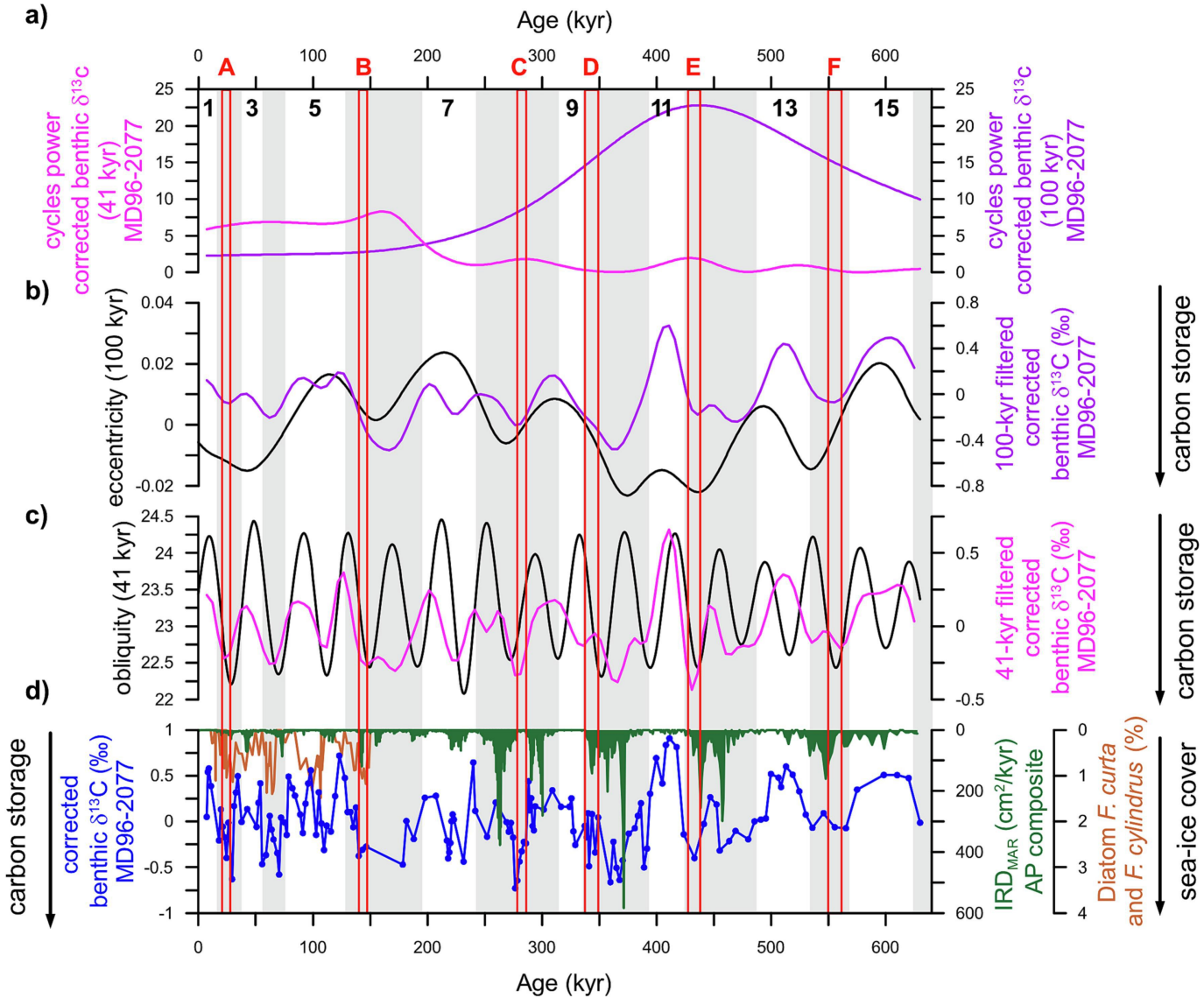
a)
Age (kyr)
A
B
C
D
E
F
1
3
5
7
9
11
13
15
cycles power
corrected benthic δ13c
(41 kyr)
MD96-2077
cycles power
corrected benthic δ13c
(100 kyr)
MD96-2077
b)
eccentricity (100 kyr)
100-kyr filtered
corrected
benthic δ13C (‰)
MD96-2077
carbon storage
c)
obliquity (41 kyr)
41-kyr filtered
corrected
benthic δ13C (‰)
MD96-2077
carbon storage
d)
carbon storage
corrected
benthic δ13C (‰)
MD96-2077
IRDMAR (cm2/kyr)
AP composite
Diatom F. curta
and F. cylindrus (%)
sea-ice cover
Age (kyr)

Figure 8